



# Geochemical signatures of transgressive shale intervals from the 811 Ma Fifteenmile Group in Yukon, Canada: Disentangling sedimentary redox cycling from weathering alteration

Timothy M. Gibson<sup>a,\*</sup>, Marcus Kunzmann<sup>b</sup>, André Poirier<sup>c</sup>, Dirk Schumann<sup>d</sup>,  
Nicholas J. Tosca<sup>e</sup>, Galen P. Halverson<sup>a</sup>

<sup>a</sup> Department of Earth & Planetary Sciences and Geotop, McGill University, Montréal, QC H3A 0E8, Canada

<sup>b</sup> CSIRO Mineral Resources, Australian Resources Research Centre, Kensington, WA 6151, Australia

<sup>c</sup> Département des Sciences de la Terre et de l'Atmosphère and Geotop, Université du Québec à Montréal, Montréal, QC H3C 3P8, Canada

<sup>d</sup> Fibics Incorporated, 1431 Merivale Road, Lower Level, Suite 100, Ottawa, ON K2E 0B9, Canada

<sup>e</sup> Department of Earth Sciences, University of Oxford, Oxford, OX1 3AN, United Kingdom

Received 24 December 2018; accepted in revised form 10 April 2020; available online 22 April 2020

## Abstract

Despite iron and trace element proxies informing much of our insight into Earth's oxygenation history, the processes that controlled their accumulation and distribution in ancient sedimentary environments are not fully understood. Furthermore, deciphering between primary, depositional signals and oxidative weathering alteration poses a substantial challenge to reconstructing Earth's redox history using its sedimentary record. Here, we present a multi-proxy geochemical investigation of three transgressive shale intervals from the ca. 811 Ma Reefal assemblage (upper Fifteenmile Group) in Yukon, Canada to help resolve these issues. Systematic stratigraphic trends from low to high  $Fe_{HR}/Fe_T$  and  $Fe_T/Al$  compositions across shale intervals represent shoaling of a discrete redoxcline that separated oxygenated surface waters from anoxic, ferruginous deep waters during marine transgression. In some cases, these trends are followed by a symmetric fall, which represents a full “transgressive-regressive cycle” of the redoxcline. The high proportion of glauconite to total illite indicate short-term oscillating redox conditions as the redoxcline migrated across the sediment-water interface during relative sea-level rise. These conditions invigorated dissimilatory iron reduction (DIR) within anoxic sediment pore waters, which released Fe(II) into the overlying water column where it was oxidized to iron oxy(hydr)oxide and shuttled downslope. High rates of DIR within sediment replete with highly reactive iron oxy(hydr)oxide and organic matter removed isotopically light, bio-available iron, rendering the residual sediment depleted in  $Fe_T/Al$  relative to the detrital baseline and enriched in  $^{56}Fe$ . The low iron content of the detrital flux to the basin ( $Fe/Al \sim 0.3$ ) rendered the sediment susceptible to changes in its bulk  $\delta^{56}Fe$  composition by modification of its authigenic components alone and enabled fractionation from DIR to drive bulk-rock  $\delta^{56}Fe$  values up to 0.8‰. Anomalously high concentrations of redox-sensitive elements in three samples (up to 5792 ppm Cr, 586 ppm Mn, 726 ppm Mo, and 3509 ppm Ni) and their relative distribution patterns show similarities to co-enrichment due to particulate shuttling within a weakly restricted basin. However, SEM-EDS element maps and large-area BSE image mosaics show the remains of framboidal pyrite “ghosts” with secondary enrichment of redox-sensitive elements. Thus, these geochemical trends in redox-sensitive trace metals most likely reflect mobilization and re-accumulation following pyrite dissolution during outcrop weathering. The low primary pyrite content and local transformation of pyrite iron to iron oxy(hdr)oxide suggest that  $\delta^{56}Fe$  and  $Fe_{HR}/Fe_T$  data were unaltered despite indications of pyrite weathering. Ultimately, this dataset elucidates key aspects of

\* Corresponding author at: Department of Earth Sciences, Dartmouth College, Hanover, NH 03755, USA.

E-mail address: [timothy.m.gibson@dartmouth.edu](mailto:timothy.m.gibson@dartmouth.edu) (T.M. Gibson).

sedimentary redox cycling directly preceding evolutionary milestones and a major perturbation to the global carbon cycle and also provides a template for evaluating the effects of outcrop weathering on commonly used sedimentary redox proxies.  
© 2020 Elsevier Ltd. All rights reserved.

*Key words:* Iron isotopes; Trace Metals; Iron Shuttle; Neoproterozoic; Paleoredox; Shale

## 1. INTRODUCTION

Following the ca. 2460–2240 Ma Great Oxidation Event (Bekker et al., 2004), details regarding the timing and magnitude of later Proterozoic oxygenation are contentious (e.g., Planavsky et al., 2014; Sperling et al., 2015; Cole et al., 2016; Blamey et al., 2016; Gilleaudeau et al., 2016; Zhang et al., 2016a; Planavsky et al., 2016; Zhang et al., 2016b; Yueng, 2017; Canfield et al., 2018; Diamond et al., 2018; Zhang et al., 2019). Furthermore, the interim redox state and structure of the global ocean between oxygenation “events” that crudely bracket the Proterozoic Eon (2500–541 Ma) is poorly constrained beyond being predominantly ferruginous (anoxic and Fe(II)-rich) with punctuated and locally restricted periods of euxinia (anoxic and H<sub>2</sub>S-rich; Canfield et al., 2008; Planavsky et al., 2011; Poulton and Canfield, 2011; Guilbaud et al., 2015; Sperling et al., 2015). Despite discrepancies in the timing, pace, and extent of late Proterozoic oxygenation and long-lasting deep ocean ventilation, most evidence supports a scenario in which shallow marine environments have remained oxygenated since at least ca. 800 Ma and deep marine environments remained at least sporadically anoxic until at least the terminal Ediacaran Period, if not the early to middle Paleozoic Era (Canfield et al., 2007, Dahl et al., 2010; Sperling et al., 2015; Wallace et al., 2017, Lu et al., 2018). Therefore, many eukaryotic clades and early animals evolved in environments with significant redox gradients (Sperling et al., 2013; Knoll, 2014; Cohen and Macdonald, 2015; Sperling and Stockey, 2018).

As a bio-essential nutrient and geologically abundant element with multiple oxidation states, iron is intimately connected to Earth’s oxygenation history via biogeochemical redox cycling. Consequently, current models for marine redox evolution rely heavily on iron-based sedimentary proxies such as iron speciation, which has the potential to differentiate sediment deposited beneath an oxic, euxinic, or ferruginous water column (Raiswell and Canfield, 1998). Sedimentary iron isotope compositions also record dynamic processes associated with iron redox cycling through Earth’s surface environment (Johnson et al., 2002; Johnson and Beard, 2005; Anbar and Rouxel, 2007) and are sensitive to the concentration and distribution of oxygen across Earth’s surface environments (Rouxel et al., 2005; Anbar and Rouxel, 2007; Johnson et al., 2008b; Bekker et al., 2010; Planavsky et al., 2012). A compilation of bulk-rock iron isotope and iron speciation data from marine shale demonstrates a state-shift ca. 660 Ma (Kunzmann et al., 2017) that corroborates evidence for a transition in global iron cycling systematics in the middle Neoproterozoic Era, potentially related to the progressive oxygenation of the ocean-atmosphere system (Fan et al.,

2014; Zhang et al., 2015). These studies confirm the utility of sedimentary iron isotopes in conjunction with iron speciation to interrogate ancient redox conditions. However, certain aspects of these data remain enigmatic and necessitate more detailed investigations into the mechanisms that fueled Neoproterozoic iron cycling.

Global compilations of redox-sensitive trace metals also display elevated sedimentary enrichments in the Neoproterozoic Era relative to earlier in the Precambrian, which further supports an expansion of oxygenated marine environments at this time (Scott et al., 2008; Partin et al., 2013; Liu et al., 2016). Due to their low relative crustal abundances, riverine fluxes of Mo, U, V, and Cr are also generally small, and their enrichment in marine sediment is predominantly controlled by seawater redox cycling. The solubility of these redox-sensitive elements (RSEs) is a function of their local redox environment and generally increases under oxidizing conditions and decreases under reducing conditions (Emerson and Huested, 1991; Tribovillard et al., 2006). Long residence times in oxic waters promote the accumulation of aqueous Mo, U, V, and Cr species within the water column, whereas removal of these elements is maximized in sediment underlying anoxic bottom waters via diffusion and scavenging across the sediment-water interface (Mo can also be scavenged via pyrite formation within a euxinic water column). This results in RSE depletion in fully anoxic basin waters (e.g., Algeo, 2004; Algeo and Lyons, 2006).

Hence, authigenic RSE enrichments reflect the proportion of oxidizing and reducing bottom water conditions within a given body of water (i.e., within a basin if it is restricted or global ocean for marine settings; Emerson and Huested, 1991; Reinhard et al., 2013) and are maximized in modern sub-oxic to anoxic environments that are fully connected to the global ocean, such as oxygen minimum zones (OMZs) or redox-stratified basins (Brumsack, 2006). Such settings are thought to have been common throughout much of the Proterozoic Eon (e.g., Rouxel et al., 2005; Canfield et al., 2008; Johnston et al., 2010; Poulton et al., 2010; Sperling et al., 2013; Ader et al., 2014; Hardisty et al., 2014; Sperling et al., 2014; Gilleaudeau and Kah, 2015; Cox et al., 2016a).

Considering the influential role iron and redox sensitive trace metal proxies play in our understanding of ancient redox conditions, establishing the specific depositional and alteration processes governing their composition in sedimentary rocks is necessary to accurately reconstruct Earth’s secular redox evolution. This is especially pertinent for unravelling redox changes through the Proterozoic Eon when a drastically different redox landscape with highly heterogeneous aqueous iron and trace metal distributions may have governed processes that cannot be easily under-

stood through modern analogs. In addition, the redox-sensitive nature of these proxies renders them susceptible to alteration through oxidative weathering. Therefore, it is critical to be able to disentangle the effects of post-depositional alteration due to oxidative weathering from ancient sedimentary or early diagenetic processes.

Sperling et al. (2013) reconstructed paleo-redox conditions from seven stratigraphic sections across a ~30 km-long basin transect of the ca. 811 Ma Reefal assemblage, upper Fifteenmile Group, in Yukon, Canada, using iron speciation and redox-sensitive element abundances. This data revealed a stratified water column whereby largely ferruginous deep waters were overlain by surface waters in continental shelf environments that were sufficiently oxygenated to support early metazoan metabolisms (>1% present atmospheric level of O<sub>2</sub>). The current investigation builds upon the work of Sperling et al. (2013) by integrating sequence stratigraphy with a high-resolution, multi-proxy shale geochemical dataset from a single stratigraphic section of the upper Fifteenmile Group. See Electronic Annex for more details regarding the interpretive framework of this study.

Here, we integrate bulk-rock trace element, iron isotope, iron speciation, and X-ray diffraction (XRD) data from 43 shale samples spanning three transgressive shale intervals from the Reefal assemblage in the Ogilvie Mountains of Yukon, Canada. We also provide large-area Scanning Electron Microscopy (SEM) imaging and energy-dispersive spectroscopic (EDS) analyses of select samples. All data from this study are interpreted within a sequence stratigraphic framework. This investigation seeks to provide an in-depth assessment of the relative contribution from sedimentary redox processes versus post-depositional oxidative weathering on the chemical composition of these samples.

## 2. GEOLOGICAL SETTING

The Tonian (ca. 850–800 Ma) Fifteenmile Group was deposited within a series of tectonically active sub-basins in response to crustal attenuation and thermal subsidence in northwest Laurentia, perhaps during the early stages of the breakup of Rodinia (Macdonald et al., 2012). These strata outcrop in three erosional inliers from central Yukon, Canada to eastern Alaska, USA and correlate with the Little Dal Group of the Mackenzie Mountains Supergroup in the Wernecke and Mackenzie Mountains to the east (Macdonald and Roots, 2010). This study investigates the upper Fifteenmile Group in the Coal Creek inlier in the central Ogilvie Mountains, Yukon (Fig. 1.) Although there has been no systematic investigation into the thermal and/or maturation history of these units, field and petrographic observations suggest they experienced a maximum of lower greenschist facies pressure-temperature conditions (Kunzmann et al., 2014; Macdonald et al., 2018). As we discuss below, the relatively high proportion of glauconite to total illite polytypes further constrains burial diagenetic conditions. Hydrothermal experiments and radiogenic Ar retention measurements have established the upper limit for the thermal stability of glauconite at ~320 °C (Velde & Odin, 1975; Odin et al., 1977), consistent with lower

greenschist facies metamorphism. Temperatures much beyond this would be expected to rapidly convert glauconite to biotite and/or muscovite (Velde & Odin, 1975; Odin et al., 1977).

The Fifteenmile Group is separated into lower and upper subgroups which are further subdivided into four units (Macdonald et al., 2011; Halverson et al., 2012). The age of the lower Fifteenmile Group, comprising the Gibben and Chandindu formations (Halverson et al., 2012; Kunzmann et al., 2014), is younger than ca. 1000 Ma as constrained by detrital zircon U-Pb ages from the Hart River inlier (Rainbird et al., 1997). Laterally variable, mixed siliciclastic and carbonate units of the basal Gibben formation unconformably overlie the <ca. 1380 Ma Pinguicula Group (Medig et al., 2012) and shoal upward into carbonate dominated facies (Halverson et al., 2012; Macdonald et al., 2012). A prominent, mud-cracked exposure surface marks the contact with the Chandindu Formation, which contains numerous fine-grained, mixed siliciclastic-carbonate cycles with locally abundant stromatolite bioherms (Kunzmann et al., 2014). Crustal extension and normal faulting through lower Fifteenmile Group deposition generated topographic relief and, at least locally, a NNW-deepening trend (in present coordinates) (Macdonald et al., 2012).

The contact with the upper Fifteenmile Group is marked by a ubiquitous flooding surface at the transition from heterolithic facies of the Chandindu Formation to thick shale and dolostone packages of the Reefal assemblage (Halverson et al., 2012; Kunzmann et al., 2014). Primary magmatic zircon within an ash bed in the upper Reefal assemblage provides a U-Pb depositional age of 811.5 ± 0.1 Ma (Macdonald et al., 2010). The 500–1700 m-thick Reefal assemblage contains predominantly peritidal microbial facies that grade distally into basinal shale, which are interpreted to represent stromatolite reefs prograding to the NNW into a shale basin (Halverson et al., 2012). Thick platform-to-slope carbonate successions are interbedded with prominent black to gray shale and siltstone intervals representing transgressive and regressive systems tract deposits (Halverson et al., 2012; Macdonald et al., 2012; Sperling et al., 2013).

Negative carbonate carbon isotope ( $\delta^{13}\text{C}$ ) excursions directly above the ca. 811 Ma ash bed in the upper Reefal assemblage record the onset of the globally synchronous Bitter Springs carbon isotope stage (Halverson et al., 2005; Halverson et al., 2007; Macdonald et al., 2012; Swanson-Hysell et al., 2015). Given the lack of any discernable depositional hiatus, the entire Reefal assemblage is likely younger than 850 Ma (Macdonald et al., 2010). The Fifteenmile Group culminates with the Craggy dolostone, which comprises massive, regionally extensive, silicified dolograstone, coarse, intra-formational conglomerate, and floatstone with minor microbialite and low-relief stromatolite facies overlying the uppermost black shale unit of the Reefal assemblage (Macdonald and Roots, 2010; Macdonald et al., 2011). The Craggy dolostone records renewed extension in the Fifteenmile basin and establishment of isolated carbonate platforms adjacent to topographic lows that accumulated coarse carbonate debris

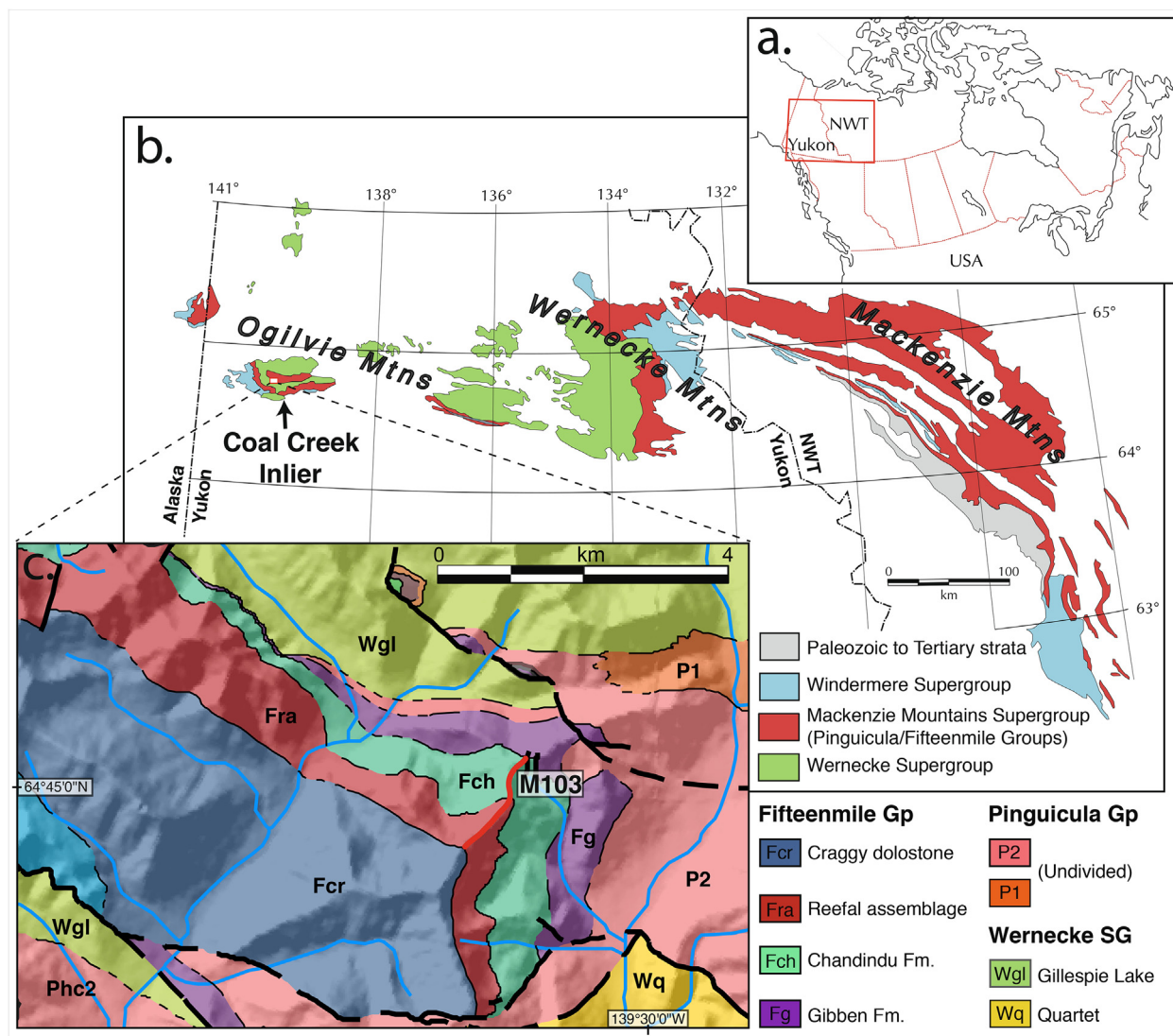


Fig. 1. Overview of the study area. A: Location map showing the area in (b) outlined in red. B: Exposures of Proterozoic strata in the Ogilvie, Wernecke, and Mackenzie mountains in Yukon and the Northwest Territories (NWT) modified from [Macdonald et al. \(2012\)](#). C: Geological map showing the location of stratigraphic section M103 (red) modified from [Strauss et al. \(2014\)](#). Abbreviations for map units are described to the right. Thin lines are stratigraphic contacts, bold lines are faults and dashed lines are inferred contacts or faults. (For interpretation of the references to colour in this figure legend, the reader is referred to the web version of this article.)

shed from platform margins. The uppermost Fifteenmile Group is variably truncated by the sub-Callison Lake Formation unconformity, above which a Re-Os age of  $751.2 \pm 5.1$  Ma provides a minimum age for the Fifteenmile Group ([Rooney et al., 2015](#); [Strauss et al., 2015](#)).

### 3. MATERIALS AND METHODS

#### 3.1. Samples

Black and dark gray shale to silty shale samples were excavated from the outcrop every  $\sim 50$  cm across three shale intervals through the course of measuring and logging a nearly entirely exposed stratigraphic section (M103) of the Chandindu Formation and Reefal assemblage (Upper Fif-

teenmile Group) in the Coal Creek inlier, Yukon, Canada ([Fig. 1](#);  $N64^{\circ}45'17.0''$ ,  $W139^{\circ}32'13.7''$ ). Sampling targeted the finest grained material, avoiding any coarser grained horizons or areas that showed evidence for structural or hydrothermal alteration. Samples were powdered in a chrome-steel ring mill for a maximum of 30 seconds. [Sperling et al. \(2013\)](#) found that this method introduced minimal contamination to samples. The container was decontaminated by running quartz sand and cleaning with ethanol between samples.

This study presents new iron speciation, iron isotope, and major and trace elemental abundance data from 18 shale samples. We also provide new major and trace elemental abundance data from an additional 27 samples for which iron speciation, iron isotope, and Fe and Al elemen-

tal abundance data was published by [Kunzmann et al. \(2017\)](#). Pearson's correlation coefficients ( $r$ ) were used to assess statistical associations between geochemical variables. In all cases a significance threshold of  $p < 0.01$  was implemented. Although some of the data presented herein were previously published as part of a global Neoproterozoic Fe isotope dataset ([Kunzmann et al., 2017](#)), this is the first time these data are investigated within their stratigraphic context. Shale samples span three stratigraphic intervals (Fig. 2), described in stratigraphic order: (1) the first interval spans 18.5 m (between 284.0–302.5 m stratigraphic height) and comprises 16 samples (M103-380.3 to M103-398.9); (2) the second spans 9.0 m (354.0–363.0 m) and comprises 19 samples (M103-450.0 to M103-459.3); (3) and the third interval spans 4.5 m (378.9–383.4 m) and contains 10 samples (M103-475.2 to M103-479.7).

### 3.2. Iron speciation

Iron speciation analyses followed methods outlined in [Poulton and Canfield \(2005\)](#). Sequential extraction of oper-

ationally defined carbonate-bound, ferric oxide-bound, and magnetite-bound iron was conducted on the same 150 mg of powdered shale for each sample. First, iron associated with carbonate minerals, such as ankerite, siderite, or ferrous dolomite was extracted by reacting samples with a solution of 1 M sodium acetate buffered with acetic acid to pH 4.5 on a shaking table for 48 h at 50 °C. Second, iron bound to oxy(hydr)oxides, such as goethite, hematite, or lepidocrocite, was extracted using a 50 g/l sodium dithionite solution buffered with 0.35 M acetic acid and 0.2 M sodium citrate to pH 4.8 on a shaking table at room temperature for 2 h. Third, iron associated with mixed-valence phases like magnetite was extracted using a 0.2 M ammonium oxalate — 0.17 M oxalic acid solution buffered with ammonium hydroxide to pH 3.2 for 6 hours on a shaking table at room temperature. Leachates from these extractions were diluted with 2% HNO<sub>3</sub> and analyzed using a Thermo Scientific iCAP 6000 series ICP-OES. Finally, pyrite iron content was determined gravimetrically (assuming FeS<sub>2</sub> stoichiometry) by trapping the sulfide liberated during CrCl<sub>2</sub> reduction as Ag<sub>2</sub>S ([Canfield et al., 1986](#)). The precision of

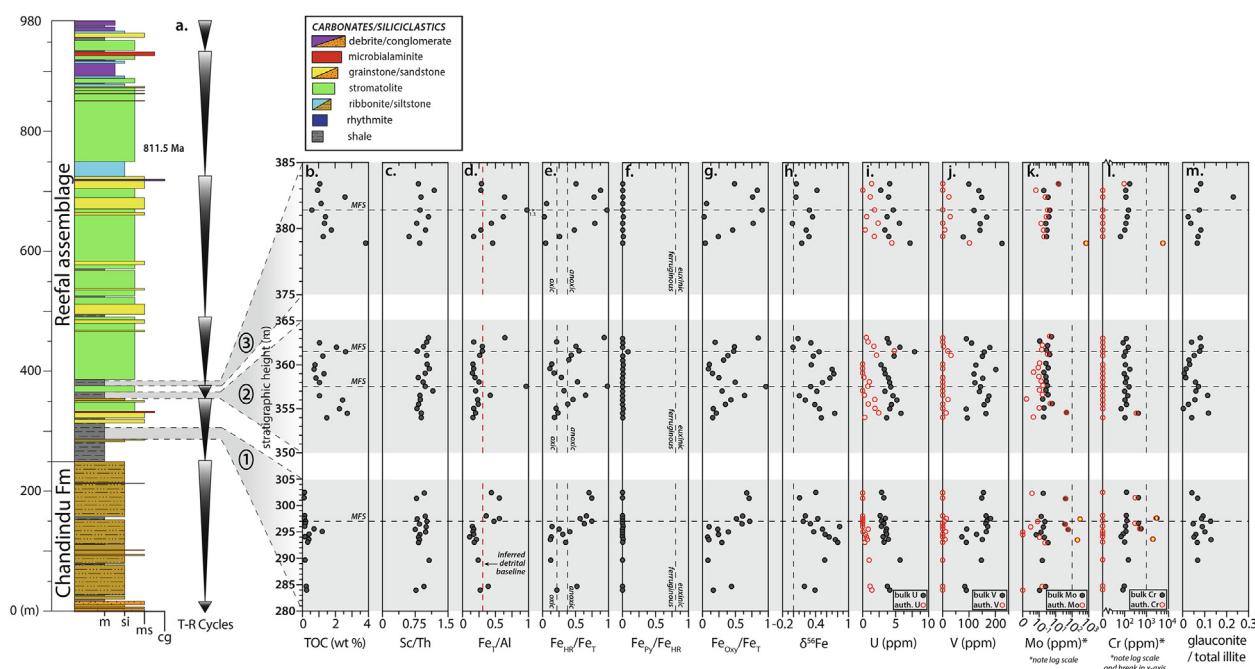


Fig. 2. Stratigraphic column and geochemical data from the three shale intervals (1–3) of the Reefal assemblage, upper Fifteenmile Group. U–Pb age of 811.5 from tuff in correlative section from [Macdonald et al. \(2010\)](#). A: Sequence stratigraphic interpretation for the Chandindu Formation and Reefal assemblage showing transgressive-regressive (T–R) cycles as inverted triangles. B: Total organic carbon content (% TOC). MFS—maximum flooding surface. C: Ratio of Scandium to Thorium (Sc/Th). D: Ratio of total iron to aluminum (Fe<sub>T</sub>/Al). Red dashed line is the inferred detrital baseline (Fe<sub>T</sub>/Al ~ 0.3; see Discussion) for this basin from this study. E: Ratio of highly reactive iron to total iron (Fe<sub>HR</sub>/Fe<sub>T</sub>). Vertical dashed lines delineate samples deposited under oxic conditions (Fe<sub>HR</sub>/Fe<sub>T</sub> < 0.22) and those deposited under anoxic conditions (Fe<sub>HR</sub>/Fe<sub>T</sub> > 0.38) ([Raiswell and Canfield, 1998](#); [Poulton and Raiswell, 2002](#)). The area between 0.22 and 0.38 is equivocal, meaning samples within this range may have been deposited under oxic or anoxic conditions ([Poulton and Canfield, 2011](#); [Sperling et al., 2013](#)). F: Ratio of pyrite iron to highly reactive iron (Fe<sub>Py</sub>/Fe<sub>HR</sub>). Samples with ratios > 0.8 reflect deposition within a euxinic water column ([Andersen and Raiswell, 2004](#)). G: Ratio of iron oxy(hydr)oxide to total iron (Fe<sub>Ox</sub>/Fe<sub>T</sub>). H: Bulk shale iron isotope composition (δ<sup>56</sup>Fe) in ‰. I–L: Bulk U, V, Mo, and Cr contents (black circles) and calculated authigenic enrichments (auth. X; red circles). Authigenic fractions were calculated by subtracting the detrital fraction from the bulk concentration. Three samples with Mo > 100 ppm and Cr > 1000 ppm (filled yellow circles) are deemed non-primary and interpreted to reflect enrichment related to oxidative weathering. The detrital fraction is calculated as: X<sub>detrital100</sub> = (X/Al)<sub>UCC</sub> × Al<sub>sample</sub>. M: Ratio of glauconite to total illite. (For interpretation of the references to colour in this figure legend, the reader is referred to the web version of this article.)

sequentially extracted iron was better than 5%, based on duplicate analyses and five internal standards comprising various Neoproterozoic shale units. See Electronic Annex for more details regarding the interpretive framework for iron speciation data from this study.

### 3.3. Bulk sample digestion

Approximately 1 g of powder from each sample was combusted at 550 °C for 5 h to oxidize organic matter prior to digestion using double distilled acids. Approximately 40 mg of combusted sample powder was first digested in Teflon beakers with a mixture of 2 ml 6 M HCl:1 ml 50% HF:0.5 ml 7 M HNO<sub>3</sub> at ~80 °C for 48 h. Samples were then dried down on a hot plate to near completion before adding 0.5 ml of 7 M HNO<sub>3</sub> to prevent the formation of Ca fluoride. Aqua regia, (0.65 ml 7 M HNO<sub>3</sub>:2 ml 6 M HCl) was then added to the samples and allowed to react at ~80 °C for 24 h. After the samples were dried down again, they were taken up in 2 ml 6 M HCl and aliquots were diluted with 2% HNO<sub>3</sub> for iron isotope analyses. Samples were then dried down and taken up in 0.5 ml 7 M HNO<sub>3</sub> and dried down a final time. This step ensured the removal of Cl to avoid mass interferences during ICP analyses. Samples were finally taken up in 7 M HNO<sub>3</sub> and aliquots were diluted with 2% HNO<sub>3</sub> for ICP-OES (major elements) and ICP-MS (trace elements) analyses.

### 3.4. Iron isotopes

Iron isotope analyses followed methods outlined in Kunzmann et al. (2017). Following bulk digestion, iron was purified using standard ion exchange column chromatography in a clean laboratory following procedures described in Sossi et al. (2015). Iron isotope measurements were performed on a NuPlasma II MC-ICP-MS with a high-resolution slit ( $M/\Delta M > 7000$ ) to resolve interferences (e.g., ArO) in classic standard bracketing analytical scheme. The use of an Aridus II desolvating membrane permitted enhanced sensitivity. Typical reproducibility of triplicate measurements of a sample was  $\pm 0.05\%$  during the course of this study. NIST SRM 3126a was used for standard bracketing due to limited IRMM-14 availability. All analyses are reported in delta ( $\delta$ ) notation in relation to IRMM-14 (Eq. (1); Dauphas and Rouxel, 2006), and where necessary renormalized from NIST SRM 3126a measurements (Eq. (2)) as determined by Rouxel and Auro (2010):

$$\delta^{56}\text{Fe} = \left[ \frac{\left(\frac{56\text{Fe}}{54\text{Fe}}\right)_{\text{sample}}}{\left(\frac{56\text{Fe}}{54\text{Fe}}\right)_{\text{IRMM-14}} - 1} \right] \times 1000 \quad (1)$$

$$\delta^{56}\text{Fe} = \left( \left[ \frac{\left(\frac{56\text{Fe}}{54\text{Fe}}\right)_{\text{sample}}}{\left(\frac{56\text{Fe}}{54\text{Fe}}\right)_{\text{SRM 312a}} - 1} \right] \times 1000 \right) - 0.4 \quad (2)$$

Using the conversion equation adapted from Craig (1957):

$$\begin{aligned} & \delta^{56}\text{Fe}(\text{sample} - \text{SRM 3126a}) \\ &= \delta^{56}\text{Fe}(\text{sample} - \text{IRMM-14}) \\ &+ \delta^{56}\text{Fe}(\text{IRMM-14} - \text{SRM 3126a}) + 10^{-3} \\ &\times \delta^{56}\text{Fe}(\text{sample} - \text{IRMM-14}) \\ &\times \delta^{56}\text{Fe}(\text{IRMM-14} - \text{SRM 3126a}) \end{aligned} \quad (3)$$

In Eq. (3), (sample–SRM 3126a) and (sample– IRMM-14) are analyses of a sample relative to SRM 3126a and IRMM-14 standards, and (IRMM-14–SRM 3126a) is the analysis of IRMM-14 relative to SRM 3126a. Reference material BHVO-2 prepared and analyzed along with our samples yielded an average  $\delta^{56}\text{Fe}$  value of  $0.06 \pm 0.03\%$  (1SE) and  $\delta^{57}\text{Fe}$  value of  $0.11 \pm 0.04\%$  (1SE), which are within the range reported in the GeoReM database (Jochum et al., 2005). An in-house hematite standard was also routinely prepared and analyzed, yielding standard errors of 0.03‰ for  $\delta^{56}\text{Fe}$  and 0.04‰ for  $\delta^{57}\text{Fe}$ . Iron isotope data ( $\delta^{56}\text{Fe}$  and  $\delta^{57}\text{Fe}$ ) from this study follow the mass-dependent fractionation line as shown in Fig. S1. See Electronic Annex for more details regarding the interpretive framework for iron isotope data from this study.

### 3.5. Major and trace elements

Major and trace elemental concentrations were determined following methods outlined in Kunzmann et al. (2015). After bulk sample digestion and dilution with 2% HNO<sub>3</sub>, major element concentrations were measured on a Thermo Scientific iCAP 6000 series ICP-OES and trace element concentrations on a Thermo Finnigan iCAP Q ICP-MS. Accuracy and precision were monitored by duplicate sample analyses, as well as certified reference materials BHVO-2 (basalt), SCO-1 (black shale), and SCHS-1 (black shale). Reproducibility was better than  $\pm 5\%$  for both duplicate analyses and certified standard values.

The authigenic fraction ( $X_{\text{auth}}$ ) of a given trace element concentration was calculated as:

$$X_{\text{auth}} = X_{\text{sample}} - X_{\text{det}} \quad (4)$$

where  $X_{\text{sample}}$  is the bulk concentration of the element measured in a sample, and  $X_{\text{det}}$  is the detrital fraction of the element, calculated as:

$$X_{\text{det}} = (X/\text{Al})_{\text{UCC}} \times \text{Al}_{\text{sample}} \quad (5)$$

Then  $(X/\text{Al})_{\text{UCC}}$  is the average ratio of the trace element (X) to Al concentrations (ppm/ppm) in the upper continental crust as estimated from McLennan (2001). Enrichment factors ( $X_{\text{EF}}$ ) were calculated as:

$$X_{\text{EF}} = (X/\text{Al})_{\text{sample}} / (X/\text{Al})_{\text{UCC}} \quad (6)$$

where  $(X/\text{Al})_{\text{sample}}$  represents the ratio of trace element (X) and Al concentrations (ppm/ppm) measured in a sample, and  $(X/\text{Al})_{\text{UCC}}$  is that ratio in the upper continental crust as estimated from McLennan (2001). See Electronic Annex for more details regarding the interpretive framework for RSE data from this study.

### 3.6. Total organic carbon and sulfur

Total organic carbon (TOC) and sulfur (S) concentrations were determined using an *Eltra* CS-800 Carbon-Sulfur Analyzer following methods outlined in [Kunzmann et al. \(2015\)](#). Between 1 and 1.5 g of each sample was leached twice in 2 M HCl for 12 h to dissolve carbonate minerals prior to TOC measurements. In samples with higher carbonate content, a third dissolution was necessary. After rinsing with distilled water, samples were dried overnight before analysis, and C-S contents were related to sample mass to determine concentrations. Both TOC and S measurements were run in duplicate with standard bracketing with reference material SLg-1. Accuracy and reproducibility were monitored via duplicate analyses and the certified reference material, SLg-1 (black shale). Reproducibility was better than  $\pm 8\%$ .

### 3.7. X-ray diffraction (XRD)

To determine mineralogical compositions, powder X-ray diffraction (XRD) was performed at the University of Oxford on bulk powdered shale samples. Sample powders were first ground by hand in an agate mortar and pestle. Powders were mounted as a slurry mixed with anhydrous ethanol on a low background scattering silicon crystal substrate and analyzed using a Panalytical Empyrean Series 2 diffractometer operating at 40 kV and 40 mA with a Co K $\alpha$  source. Samples were continuously rotated during analysis and data were acquired from 5–85 degrees 2-theta using a step size of 0.026 degrees. Sample height displacement corrections were performed using the positions of quartz reflections as internal standards. Peaks were identified and matched against the Powder Diffraction File-4+ database (International Center for Diffraction Data), using the reference intensity ratio method ([Snyder and Bish, 1989](#)). In addition, clay mineral speciation and polytype identification was performed by scanning from 69–75 degrees 2-theta using a step size of 0.026 degrees and count rates of 200 seconds per step. In this way, mineral-specific 060 reflections were quantified, and clay mineral abundances expressed as a relative fraction of the total clay content because the area of these reflections has been shown to correspond in a linear fashion to clay mineral abundance ([Srodon et al., 2001](#)). Effective detection limits for illite and glauconite are  $\sim 0.3\%$ , and the detection limit for glauconite to total illite ratios is  $\sim 0.009$ .

### 3.8. Light microscopy and scanning electron microscopy (SEM)

Samples M103-450.8, M103-458.3, and M103-475.2 were embedded in 25 mm diameter epoxy molds and polished on a TECHPREP™ polishing system. The final polish was done with 0.05  $\mu\text{m}$  colloidal silica solution. Sample M103-475.2 was additionally ion polished in a Leica EM TIC 3X large-area ion polisher. Large-area reflected-light microscopy image mosaics were acquired from sample M103-475.2 using a Zeiss AXIO Zoom.V16 light microscope. Select portions of sample M103-450 were also

imaged. The mosaics were acquired with the Zeiss software “ZEN Pro” using the Plan Apo Z 1.0/0.25 objective (FWD 60 mm) at a resolution of 410 nm/pixel with reflected light from a LED light ring mounted on the microscope objective. The entire light microscopy image mosaic of M103-475.2 consists of 218 images. Large-area Scanning Electron Microscopy (SEM) image mosaics of the samples M103-458.3 and M103-475.2 were acquired with the ZEISS Atlas 5 software by using a ZEISS SIGMA HDVP FE-SEM at Fibics Incorporated (Ottawa, Canada). See Electronic Annex for SEM imaging parameters and online access to full Atlas 5 Browser-Based Viewer datasets. The principal purpose of acquiring the large-area image mosaics was to understand the mineralogy, the mineral associations, and textures of the entire sample.

### 3.9. Energy-dispersive X-ray spectroscopy (EDS)

Energy-dispersive spectroscopic (EDS) analyses on sample M103-475.2 were carried out on a Zeiss EVO MA 15 tungsten filament SEM to evaluate the effects of pyrite weathering on sample mineralogy and elemental distribution. This instrument was equipped with two Bruker XFlash 6/30 EDS detectors and controlled using the Esprit 1.9 software. An accelerating voltage of 20 kV and a 3.7 nA probe current were used for the acquisition of EDS element maps and point analyses. The acquired element maps and point analyses were exported from the Bruker Esprit software and linked with their respective location of acquisition in the Atlas 5 Browser-Based Viewer data sets (see Electronic Annex).

## 4. RESULTS

### 4.1. Major elements and iron speciation

Sc/Th ratios fluctuate between 0.61 and 1.14 with no clear stratigraphic trends ([Fig. 2](#); [Table 1](#)).  $\text{Fe}_T/\text{Al}$  ratios range from 0.15 to 1.3 but are mostly  $< 0.4$  ([Table 1](#)), which is consistent with other Reefal assemblage data sampled throughout the basin from [Sperling et al. \(2013\)](#). Of the 45 samples analyzed for iron speciation, 25 (56%) have  $\text{Fe}_{\text{HR}}/\text{Fe}_T$  values greater than 0.38 (anoxic), 8 (18%) are less than 0.22 (oxic), and 12 (27%) are between 0.22 and 0.38 (ambiguous; [Table 1](#)). All samples from this study have  $\text{Fe}_{\text{Py}}/\text{Fe}_{\text{HR}}$  ratios less than 0.1, from below detection limit up to 0.084 ([Figs. 2 and 3](#); [Table 1](#)). Iron oxy(hydr)oxides comprise the majority of all reactive iron in every sample, as demonstrated by  $\text{Fe}_{\text{Oxy}}/\text{Fe}_{\text{HR}}$  ratios between 0.58 and 0.98 and a mean of 0.88 ([Table 1](#)).  $\text{Fe}_T/\text{Al}$  ratios show a moderate positive correlation with  $\text{Fe}_{\text{HR}}/\text{Fe}_T$  ( $r = 0.68$ ,  $p(\alpha) < 0.0001$ ; [Fig. 3](#)).

$\text{Fe}_T/\text{Al}$  and  $\text{Fe}_{\text{HR}}/\text{Fe}_T$  iron speciation data display systematic stratigraphic variation indicative of transitions from “oxic” to “anoxic” depositional environments and, in some cases back to “oxic” values across each shale interval ([Fig. 2](#)). Because iron oxy(hydr)oxides comprise the majority of  $\text{Fe}_{\text{HR}}$ , these trends are also mimicked by  $\text{Fe}_{\text{Oxy}}/\text{Fe}_T$ . In the first sampled shale interval (280–305 m)  $\text{Fe}_T/\text{Al}$ ,  $\text{Fe}_{\text{HR}}/\text{Fe}_T$ , and  $\text{Fe}_{\text{Oxy}}/\text{Fe}_T$  values are relatively low between

Table 1

Shale total organic carbon (TOC), major and minor elemental concentration, iron speciation, glauconite to illite ratio, and iron isotope data. Redox-sensitive element concentrations (Mo, V, U, and Cr) are shown alone, normalized to TOC, and as calculated authigenic components. Authigenic fractions were calculated by subtracting the detrital fraction from the bulk concentration of the sample. The detrital fraction is calculated as:  $X_{\text{detrital}} = (X/Al)_{\text{UCC}} \times Al_{\text{sample}}$ .

Sample height	TOC	Al	Fe	Fe <sub>T</sub> /Al	Sc	Th	Sc/Th	FeCarb	FeOxy	FeMag	FePy	FeHR/FeT	FePy/FeHR	glauc/ill	<sup>56</sup> Fe	1 SE	<sup>57</sup> Fe	ISE	Mo	Mo/TOC	auth Mo	V	V/TOC	auth V	U	U/TOC	auth U	Cr	Cr/TOC	auth Cr	
(m)	(%)	(wt. %)	(wt. %)	(ppm)	(ppm)	(ppm/ppm)	(%)	(%)	(%)	(%)	(%)	(%)	(%)	(%)	(%)	(%)	(%)	(%)	(ppm)	(ppm/%)	(ppm)	(ppm)	(ppm/%)	(ppm)	(ppm/%)	(ppm)	(ppm)	(ppm/%)	(ppm)		
479.7	383.4	1.08	8.01	2.30	0.29	15.49	18.81	0.82	0.01	1.11	0.05	0.00	0.51	0.00	0.11	0.0541	0.1151	0.1063	0.1151	15.22	14.08	14.12	98.91	91.49	0.00	4.11	3.80	1.34	177.20	164.40	94.52
479.2	382.9	0.95	9.61	2.68	0.28	18.34	15.54	1.18	0.05	2.22	0.09	0.00	0.88	0.00	0.09	0.4301	0.0382	0.6428	0.0382	1.94	2.05	0.62	137.01	144.55	0.00	2.75	2.91	0.00	99.53	124.52	0.30
478.7	382.4	2.61	8.09	5.17	0.64	16.51	18.81	0.88	0.05	3.93	0.08	0.02	0.79	0.01	0.31	0.0467	0.0383	0.0887	0.0383	3.46	1.33	2.35	147.78	56.62	23.38	3.93	1.51	1.14	83.54	46.05	0.07
478.2	381.9	1.16	-	-	-	-	-	-	0.01	0.91	0.03	0.00	0.06	0.00	-	-	-	-	-	-	-	-	-	-	-	-	-	-	-	-	-
477.7	381.4	0.60	8.25	10.77	1.31	17.81	20.63	0.86	0.01	9.72	0.81	0.00	0.98	0.00	0.10	-	-	-	-	4.38	7.33	3.24	118.79	198.92	0.00	4.64	7.78	1.79	80.80	262.96	0.00
477.2	380.9	1.41	9.01	5.57	0.62	18.88	18.02	1.05	0.02	0.13	0.02	0.00	0.03	0.01	0.03	0.3466	0.0566	0.5636	0.0566	3.92	2.78	2.69	167.04	118.12	28.49	3.71	2.63	0.60	98.25	97.55	5.28
476.7	380.4	1.36	9.36	4.08	0.44	16.93	21.77	0.78	0.01	3.13	0.11	0.00	0.80	0.00	0.05	-0.0187	0.0365	-0.0586	0.0365	2.58	1.90	1.30	142.02	104.56	0.00	5.58	4.11	2.34	86.27	87.88	0.00
476.2	379.9	1.78	8.67	2.42	0.28	14.59	14.82	0.98	0.03	1.10	0.03	0.00	0.48	0.00	0.11	0.2323	0.0407	0.3036	0.0407	3.03	1.70	1.83	141.70	79.72	8.24	3.38	1.90	0.37	84.95	60.38	-4.60
475.7	379.4	1.29	6.32	1.09	0.17	10.78	17.74	0.61	0.01	0.26	0.02	0.00	0.26	0.01	0.09	0.2829	0.0471	0.4511	0.0471	2.85	2.21	1.98	78.30	60.89	0.00	3.96	3.08	1.77	64.74	52.81	0.00
475.2	378.9	3.85	8.04	3.67	0.46	14.05	16.53	0.85	0.00	0.15	0.02	0.00	0.05	0.00	0.09	0.1510	0.1052	0.2252	0.1052	726.45	188.52	725.34	225.26	58.46	101.49	7.19	1.87	4.41	5792.00	1516.16	5708.95
459.3	363.0	-	9.11	5.79	0.64	15.87	15.33	1.04	0.01	4.87	0.49	0.00	0.93	0.00	0.11	0.0835	0.0336	0.0831	0.0336	5.07	-	3.82	90.33	-	0.00	3.74	-	0.59	85.06	-	0.00
458.8	362.5	1.05	9.14	1.53	0.17	14.19	14.25	1.00	0.01	0.29	0.02	0.00	0.21	0.00	0.05	0.3178	0.1464	0.4536	0.1464	0.99	0.95	0.00	109.70	104.54	0.00	4.00	3.81	0.84	82.57	83.76	0.00
458.3	362.0	2.07	11.41	3.43	0.30	18.75	20.13	0.93	0.01	1.65	0.07	0.00	0.50	0.00	0.11	-0.0086	0.0317	-0.1206	0.0317	3.01	1.45	1.44	179.08	86.47	3.53	5.67	2.74	1.72	128.17	72.31	10.37
457.8	361.5	2.63	8.99	2.72	0.30	14.91	18.91	0.79	0.01	1.28	0.08	0.13	0.55	0.08	0.10	0.4664	0.0738	0.6939	0.0738	2.53	0.96	1.29	157.62	59.98	19.27	7.90	3.01	4.79	92.16	43.28	0.00
457.3	361.0	1.25	7.75	2.03	0.26	15.80	15.83	1.00	0.02	0.78	0.08	0.00	0.43	0.01	0.07	0.3625	0.0289	0.5697	0.0289	3.97	3.17	2.91	150.55	120.15	31.25	4.80	3.83	2.11	82.32	77.64	2.27
456.8	360.5	-	-	1.77	-	-	-	-	0.03	0.56	0.11	0.00	0.40	0.01	0.04	-	-	-	-	-	-	-	-	-	-	-	-	-	-	-	-
456.3	360.0	0.78	10.12	1.66	0.16	16.05	15.91	1.01	0.02	0.17	0.04	0.00	0.14	0.01	0.04	0.3222	0.0605	0.5327	0.0605	2.37	3.05	0.98	125.84	162.09	0.00	2.82	3.64	0.00	99.29	143.35	0.00
455.8	359.5	0.72	17.34	2.94	0.17	23.30	22.00	1.06	0.02	0.26	0.05	0.00	0.11	0.00	0.02	0.7050	0.1254	1.0333	0.1254	3.19	4.41	0.81	201.33	278.50	0.00	3.28	4.54	0.00	157.33	246.66	0.00
455.3	359.0	1.32	9.99	1.53	0.15	16.42	16.92	0.97	0.01	0.23	0.02	0.00	0.17	0.01	0.01	0.7356	0.0079	1.0976	0.0079	1.79	1.36	0.42	119.10	90.55	0.00	3.44	2.62	0.00	89.05	75.88	0.00
454.8	358.5	0.83	10.74	2.04	0.19	17.50	21.55	0.81	0.01	0.50	0.06	0.00	0.28	0.00	0.02	0.6634	0.0093	0.9887	0.0093	2.34	2.84	0.87	152.48	184.72	0.00	3.94	4.77	0.22	111.17	151.20	0.31
454.3	358.0	1.05	8.91	2.23	0.25	17.95	19.58	0.92	0.02	1.10	0.06	0.00	0.53	0.00	0.08	0.5316	0.1256	0.6813	0.0401	2.42	2.31	1.20	122.24	116.56	0.00	4.12	3.93	1.03	94.20	105.53	2.21
453.8	357.5	-	9.98	9.60	0.96	21.51	22.17	0.97	0.01	9.18	0.16	0.00	0.98	0.00	0.10	0.3137	0.0184	0.3965	0.0191	2.91	-	1.54	143.47	-	0.00	4.27	-	0.81	92.71	-	0.00
453.3	357.0	-	10.13	2.06	0.20	16.99	14.87	1.14	0.02	0.61	0.04	0.00	0.32	0.00	0.08	0.4265	0.0321	0.5905	0.0115	2.36	-	0.96	139.16	-	0.00	3.40	-	0.00	89.48	-	0.00
452.8	356.5	1.04	12.48	5.28	0.42	19.31	22.71	0.85	0.02	3.35	0.07	0.00	0.65	0.00	0.15	0.1059	0.1032	0.1042	0.0171	3.14	3.02	1.43	175.36	168.46	0.00	4.62	4.43	0.30	115.31	139.11	0.00
452.3	356.0	2.45	9.75	2.25	0.23	17.51	20.34	0.86	0.02	0.96	0.05	0.00	0.46	0.00	0.07	0.2149	0.0931	0.3249	0.0931	1.50	0.61	0.16	170.39	69.51	20.42	5.21	2.13	1.84	96.19	43.89	0.00
451.8	355.5	-	10.19	2.47	0.24	17.04	20.84	0.82	0.02	0.85	0.06	0.00	0.38	0.00	0.03	0.3883	0.0779	0.5506	0.0179	5.56	-	4.16	157.15	-	0.35	4.38	-	0.85	107.16	-	1.95
451.3	355.0	2.26	6.54	1.14	0.17	11.93	15.26	0.78	0.01	0.18	0.03	0.00	0.20	0.01	0.00	0.4723	0.0398	0.7054	0.0398	1.81	0.80	0.92	89.18	39.50	0.00	4.13	1.83	1.87	64.69	31.23	0.00
450.8	354.5	2.73	9.81	2.01	0.20	15.09	17.06	0.88	0.00	0.42	0.05	0.00	0.23	0.00	0.16	0.7493	0.0922	1.1231	0.0922	40.31	14.78	38.96	164.16	60.18	13.26	5.82	2.13	2.43	433.16	158.29	331.90
450.3	354.0	1.49	9.54	1.53	0.16	14.31	16.21	0.88	0.01	0.24	0.03	0.00	0.18	0.00	0.05	0.5077	0.0448	0.7465	0.0448	1.72	1.16	0.41	93.52	62.92	0.00	3.65	2.45	0.35	95.63	71.37	0.00
398.8	302.5	0.13	10.43	4.62	0.44	18.37	19.24	0.96	0.04	3.12	0.12	0.00	0.71	0.00	0.06	0.4056	0.0151	0.5706	0.0151	1.83	14.42	0.39	154.96	1223.36	0.00	2.90	22.88	0.00	89.51	975.12	0.00
397.8	301.5	0.10	9.84	5.53	0.56	17.18	22.02	0.78	0.02	3.92	0.20	0.00	0.75	0.00	0.09	0.1116	0.0265	0.2695	0.0355	42.18	410.77	40.83	148.86	1449.59	0.00	3.23	31.41	0.00	407.73	4160.55	306.15
394.4	298.1	0.14	11.08	4.04	0.36	17.89	18.25	0.98	0.01	2.47	0.22	0.00	0.60	0.00	0.12	0.2141	0.0399	0.2486	0.0489	1.38	9.91	0.00	164.98	1181.87	0.00	2.67	19.14	0.00	94.97	861.26	0.00
393.9	297.6	0.12	10.87	6.09	0.56	18.93	23.66	0.80	0.00	3.15	0.34	0.00	0.57	0.00	0.12	0.4414	0.0229	0.6287	0.0229	326.45	2642.06	324.96	181.77	1471.13	14.59	3.46	27.98	0.00	2845.29	23838.68	2733.11
393.4	297.1	0.19	10.48	5.03	0.48	18.82	18.53	1.02	0.01	3.62	0.15	0.00	0.75	0.00	0.17	0.1776	0.0406	0.1990	0.0334	2.30	11.85	0.86	167.94	864.43	6.75	2.87	14.75	0.00	91.61	663.30	0.00
392.9	296.6	0.17	11.03	4.31	0.39	18.18	21.41	0.85	0.01	2.60	0.14	0.00	0.64	0.00	0.06	0.3073	0.0391	0.2721	0.0367	38.82	225.51	37.31	164.47	955.38	0.00	3.23	18.79	0.00	414.03	2475.40	300.18
392.4	296.1	0.14	11.29	1.75	0.15	19.03	19.00	1.00	0.04	0.17	0.04	0.00	0.15	0.01	0.12	0.8384	0.0317	1.0499	0.0268	1.88	13.05	0.33	171.10	1185.70	0.00	2.88	19.93	0.00	98.12	773.00	0.00
391.9	295.6	0.71	7.98	1.36	0.17	13.12	17.38	0.75	0.00	0.32	0.03	0.00	0.25	0.00	-	0.5259	0.0552	0.6729	0.0469	60.45	85.58	59.36	91.55	129.60	0.00	3.63	5.14	0.87	573.93	788.43	491.60
391.4	295.1	1.20	10.02	1.63	0.16	17.79	17.98	0.99	0.00	0.64	0.03	0.00	0.42	0.00	0.14	0.3689	0.0367	0.5255	0.0226	1.33	1.10	0.00									

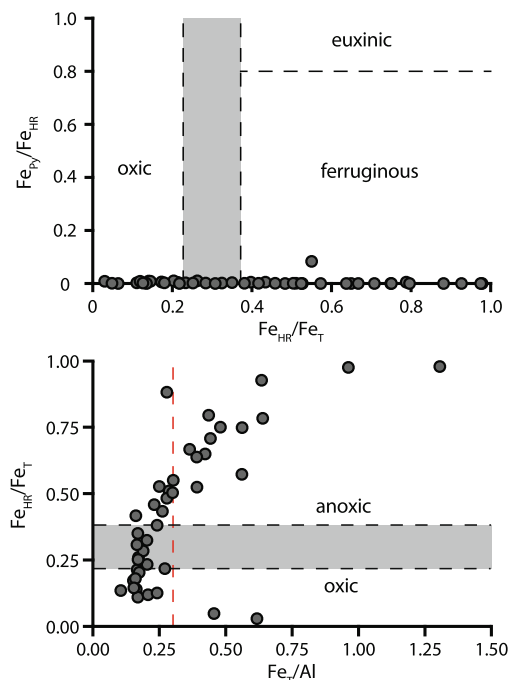


Fig. 3. Cross-plots of  $\text{Fe}_{\text{HR}}/\text{Fe}_{\text{T}}$  versus  $\text{Fe}_{\text{Py}}/\text{Fe}_{\text{HR}}$  (top) and  $\text{Fe}_{\text{T}}/\text{Al}$  versus  $\text{Fe}_{\text{HR}}/\text{Fe}_{\text{T}}$  (bottom) showing iron speciation domains corresponding to redox environments:  $\text{Fe}_{\text{HR}}/\text{Fe}_{\text{T}} < 0.22$  indicates samples may have been deposited under oxic conditions;  $\text{Fe}_{\text{HR}}/\text{Fe}_{\text{T}} > 0.38$  indicates samples were deposited under anoxic conditions (further differentiated as euxinic when  $\text{Fe}_{\text{Py}}/\text{Fe}_{\text{HR}} > 0.8$  or ferruginous if  $\text{Fe}_{\text{Py}}/\text{Fe}_{\text{HR}} < 0.8$  (Raiswell and Canfield, 1998; Poulton and Raiswell, 2002; Poulton and Canfield, 2011)). The gray shaded area ( $\text{Fe}_{\text{HR}}/\text{Fe}_{\text{T}} = 0.22\text{--}0.38$ ) is equivocal—samples within this range may have been deposited under oxic or anoxic conditions. Red dashed line is the inferred detrital baseline ( $\text{Fe}_{\text{T}}/\text{Al} \sim 0.3$ ) for this basin from this study. (For interpretation of the references to colour in this figure legend, the reader is referred to the web version of this article.)

280 and 290 m and then increase between 290 to 305 m. The second interval (350–365 m) is characterized by two symmetric peaks in  $\text{Fe}_{\text{T}}/\text{Al}$ ,  $\text{Fe}_{\text{HR}}/\text{Fe}_{\text{T}}$ , and  $\text{Fe}_{\text{Oxy}}/\text{Fe}_{\text{T}}$  values at 357.5 and 363 m, with an intervening nadir at 360 m. The stratigraphic geochemical variations from the first and second shale intervals are closely mirrored by iron isotope values ( $\delta^{56}\text{Fe}$ ), which display the inverse trends (Fig. 2). In the third shale interval (375–385 m),  $\text{Fe}_{\text{T}}/\text{Al}$  values record a gradual, linear rise to 477.7 m and symmetric fall.  $\text{Fe}_{\text{HR}}/\text{Fe}_{\text{T}}$ , and  $\text{Fe}_{\text{Oxy}}/\text{Fe}_{\text{T}}$  values follow a similar trend, but are more variable.

## 4.2. Iron isotopes

Iron isotope compositions are nearly all positive, ranging from  $-0.02\text{‰}$  to  $0.83\text{‰}$  (Table 1). Over the first and second sampled intervals,  $\delta^{56}\text{Fe}$  data mirror the stratigraphic trends of  $\text{Fe}_{\text{T}}/\text{Al}$  and  $\text{Fe}_{\text{HR}}/\text{Fe}_{\text{T}}$  data, where low  $\text{Fe}_{\text{T}}/\text{Al}$  and  $\text{Fe}_{\text{HR}}/\text{Fe}_{\text{T}}$  ratios correspond to heavy  $\delta^{56}\text{Fe}$  values and high  $\text{Fe}_{\text{T}}/\text{Al}$  and  $\text{Fe}_{\text{HR}}/\text{Fe}_{\text{T}}$  ratios to light  $\delta^{56}\text{Fe}$  values

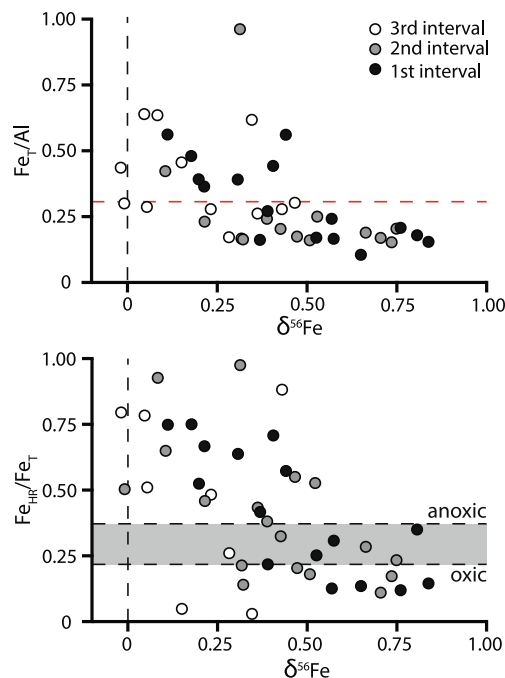


Fig. 4. Cross-plots of  $\text{Fe}_{\text{T}}/\text{Al}$  (top) and  $\text{Fe}_{\text{HR}}/\text{Fe}_{\text{T}}$  (bottom) versus  $\delta^{56}\text{Fe}$ . Red dashed line is the inferred detrital baseline from this study ( $\text{Fe}_{\text{T}}/\text{Al} \sim 0.3$ ). (For interpretation of the references to colour in this figure legend, the reader is referred to the web version of this article.)

(Fig. 2). However, this pattern is not expressed in the third interval, where  $\delta^{56}\text{Fe}$  variations are muted.  $\delta^{56}\text{Fe}$  is weakly negatively correlated with both  $\text{Fe}_{\text{T}}/\text{Al}$  and  $\text{Fe}_{\text{HR}}/\text{Fe}_{\text{T}}$  ( $r = -0.54$ ,  $p(\alpha) = 0.0002$  and  $r = -0.57$ ,  $p(\alpha) < 0.0001$ , respectively; Fig. 4).

## 4.3. Redox-sensitive trace elements

Concentrations and authigenic enrichments of U, V, Mo, and Cr are highly variable and exhibit minimal systematic stratigraphic structure (Fig. 2; Table 1). Some samples are highly enriched in Mo (up to 726 ppm) relative to the upper crustal average of 1.5 ppm and in Cr (up to 5792 ppm) relative to the upper crustal average of 83 ppm (McLennan, 2001). However, most samples contain 1 to 5 ppm Mo and 64 to 100 ppm Cr. Both U and V are less enriched than Mo or Cr, with a maximum of 8 ppm U (upper crustal average is 2.8 ppm) and 225 ppm V (upper crustal average is 107 ppm; McLennan, 2001).

There is no significant correlation between Mo/Al and TOC ( $r = 0.38$ ,  $p(\alpha) = 0.016$ ) nor Cr/Al and TOC ( $r = 0.37$ ,  $p(\alpha) = 0.019$ ), whereas V/Al and U/Al versus TOC display moderately positive correlations ( $r = 0.60$ ,  $p(\alpha) < 0.0001$  and  $r = 0.70$ ,  $p(\alpha) < 0.0001$ , respectively; Fig. 5). Furthermore, Mo versus U authigenic enrichment factors (EFs) display two distinct populations (Fig. 6). One of these groups clusters around crustal Mo and U concentrations and falls below 0.1 times the ratio of Mo to U in the modern ocean. The second group is significantly more enriched in Mo relative to U and lies above 0.3 times the

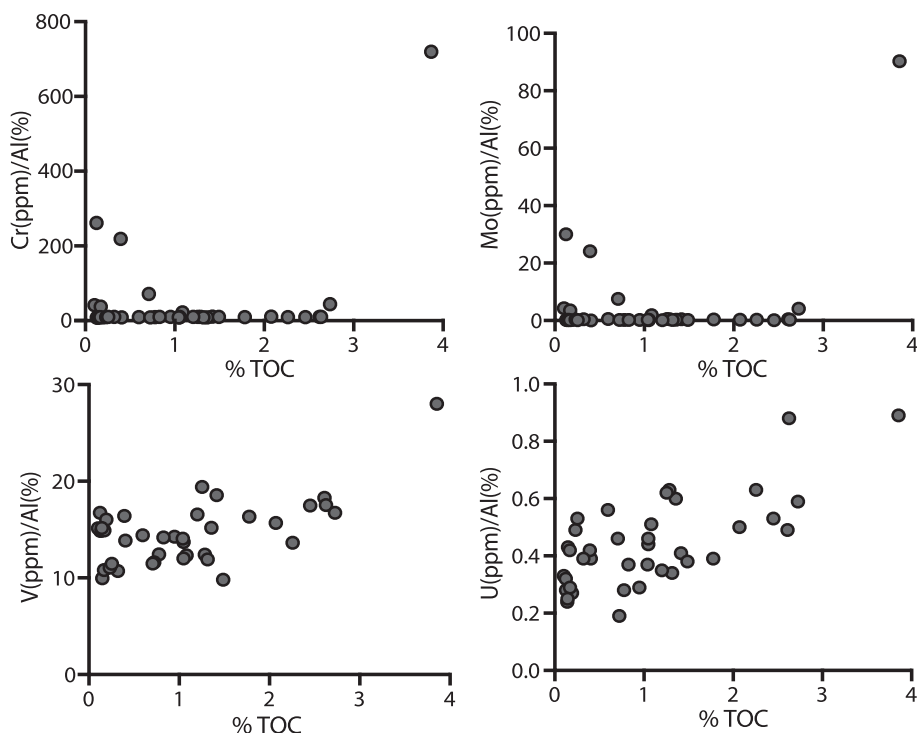


Fig. 5. Cross-plots of redox-sensitive trace element concentrations (Cr, Mo, V, and U; ppm) normalized to Al (weight %) versus TOC contents.

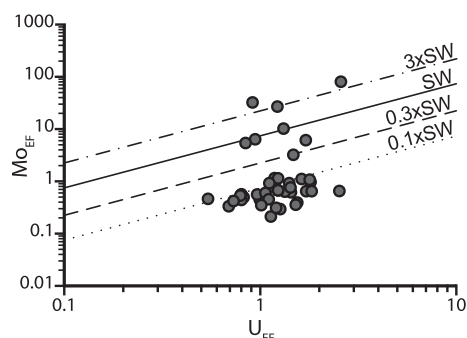


Fig. 6. Cross-plot of the U enrichment factor ( $U_{EF}$ ) and Mo enrichment factor ( $Mo_{EF}$ ) for each sample. Dashed lines represent the Mo/U molar ratio of modern seawater (SW;  $\sim 7.5$ – $7.9$ ; [Algeo and Tribouillard, 2009](#)) and ratios of the modern Mo/U molar ratios (0.1xSW; 0.3xSW; 3xSW). Enrichment factors were calculated as;  $X_{EF} = (X/Al)_{sample} / (X/Al)_{UCC}$ , where X and Al stand for the average concentrations (ppm) of element X and Al, respectively, in UCC is upper continental crust ([McLennan, 2001](#)).

modern marine Mo to U enrichments ratio, with some samples greater than 3 times this ratio.

There is a positive correlation between Mo and Mn concentrations in all samples ( $r = 0.74$ ,  $p(\alpha) < 0.0001$ ; [Fig. 7](#)). There are no correlations between Mo and U nor Mo and V concentrations ( $r = 0.35$ ,  $p(\alpha) = 0.022$  and  $r = 0.43$ ,  $p(\alpha) = 0.0044$ , respectively), but very strong positive correlations are observed between Mo and Cr and between Mo and Ni (both  $r > 0.99$ ,  $p(\alpha) < 0.0001$ ; [Fig. 8](#)). Additionally, two sample populations emerge when concentrations of Mo

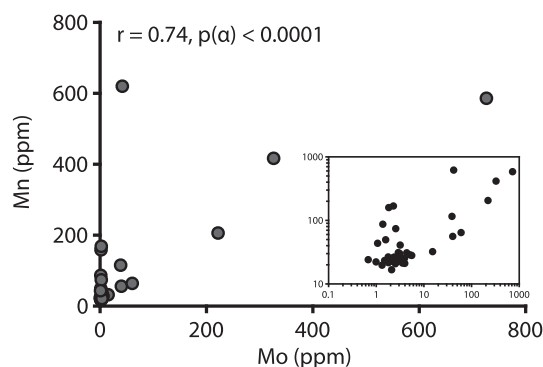


Fig. 7. Cross-plots of Mo and Mn concentrations (log scale inset).

versus Cr and Mo and Ni are plotted logarithmically. The strong positive correlations between Mo and Cr and between Mo and Ni are primarily controlled by samples with Mo concentrations  $> 10$  ppm ([Fig. 8](#)). When comparing only samples with Mo  $< 10$  ppm, there is no significant correlation between either Mo and Cr ( $r = 0.079$ ,  $p(\alpha) = 0.65$ ) nor Mo and Ni ( $r = 0.24$ ,  $p(\alpha) = 0.17$ ).

#### 4.4. Total organic carbon and sulfur

Samples contain between 0.1% and 3.8% TOC ([Table 1](#)). Total S concentrations in all samples are less than 1% by weight, with the majority less than 0.1% by weight ([Table 1](#)). Values of TOC/S are generally higher than the Holocene

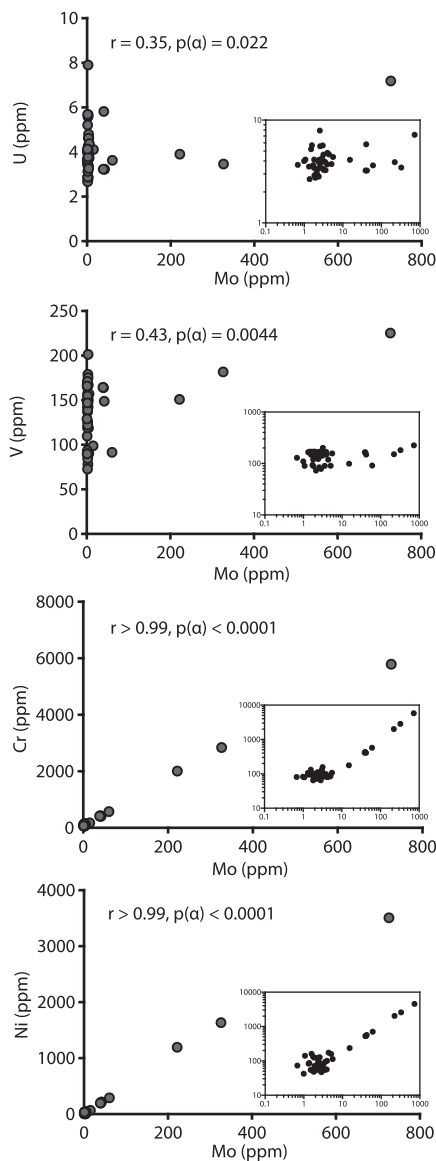


Fig. 8. Cross-plots of Mo versus U, V, Cr, and Ni (log scale inset).

“normal” marine ratio of  $\sim 2.8$  (Raiswell and Berner, 1986), the Silurian to Present “normal” marine ratio of  $\sim 1.4$  (Raiswell and Berner, 1987), and the Cambrian “normal” marine ratio of  $\sim 0.5$  (Raiswell and Berner, 1986; Fig. 9).

#### 4.5. Clay mineralogy

XRD analyses reveal that samples contain quartz, 2 M illite (i.e., detrital muscovite) and 1 M illite (diagenetic illite), and that glauconite accounts for a significant proportion of the illite polymorphs. Glauconite to total illite ratios range from 0.004 to 0.31, with an average of 0.09 and minimal stratigraphic patterns in all but the second interval, where it mimics the  $Fe_T/Al$ ,  $Fe_{HR}/Fe_T$ ,  $Fe_{Oxy}/Fe_T$ , and mirrors trends in  $\delta^{56}Fe$  data (Fig. 2; Table 1).

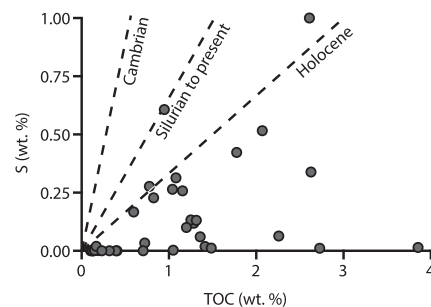


Fig. 9. Cross-plot of TOC and S (both weight %). Dashed lines represent the following TOC/S ratios: the Holocene “normal” marine ratio of  $\sim 2.8$  (Raiswell and Berner, 1986), the Silurian to Present “normal” marine ratio of  $\sim 1.4$  (Raiswell and Berner, 1987), and the Cambrian “normal” marine ratio of  $\sim 0.5$  (Raiswell and Berner, 1986).

#### 4.6. Microscopy and energy-dispersive X-ray spectroscopy (EDS)

The Atlas 5 large-area backscattered electron (BSE) image mosaics reveal the texture and mineralogy of samples M103-475.2, M103-358.3 and M103-450.8 (Fig. S2 and Electronic Annex). The large-area BSE mosaics as well as elemental maps reveal abundant framboidal and subhedral pyrite “ghosts” ranging from  $\sim 5$ – $20 \mu m$  diameter altered to iron oxy(hydr)oxide in both samples (Fig. 10 and Fig. S2E, F, G, and J). Sample M103-475.2 also contains diagenetic monazite grains, altered rutile grains, and zircon (Fig. S2B–D; Fig. S3A–C). In sample M103-475.2, EDS point analyses of the iron oxide minerals that replaced the former pyrite crystals reveal Cr, V, Ti, Ni, and Mo (detection limit is  $\sim 0.5$  weight % for long runs) in the structure of the iron oxide minerals (Fig. S2E–J; Fig. S2D, E, F and H); however, the presence of Mo is difficult to confirm since the  $L\alpha$  Mo peak overlaps with the  $K\alpha$  peak of S. This sample also contains a lead phosphate phase (possibly corkite) that occurs as secondary euhedral crystals within secondary pore spaces (Fig. S2J–M; Fig. S3K, L, N).

### 5. DISCUSSION

#### 5.1. Sequence stratigraphy

Here, as in previous studies (e.g., Halverson et al., 2012; Macdonald et al., 2012), the Reefal assemblage is interpreted to record a series of basin-wide transgressive-regressive (T-R) sequences where sequence boundaries are identified as maximum regressive surfaces (Fig. 2). For each of these sequences, stromatolite reefs that nucleated on basement highs were drowned by rapid flooding events during the transgressive systems tract that resulted in deposition of black to gray shale intervals. Samples from the present study are from three successive 10–25 m-thick such intervals. Stromatolite reefs then prograded to the NNW into adjacent shale basins during the subsequent regressive systems tract. Shale intervals are characterized by very fine-grained and finely laminated mudstones with low carbonate

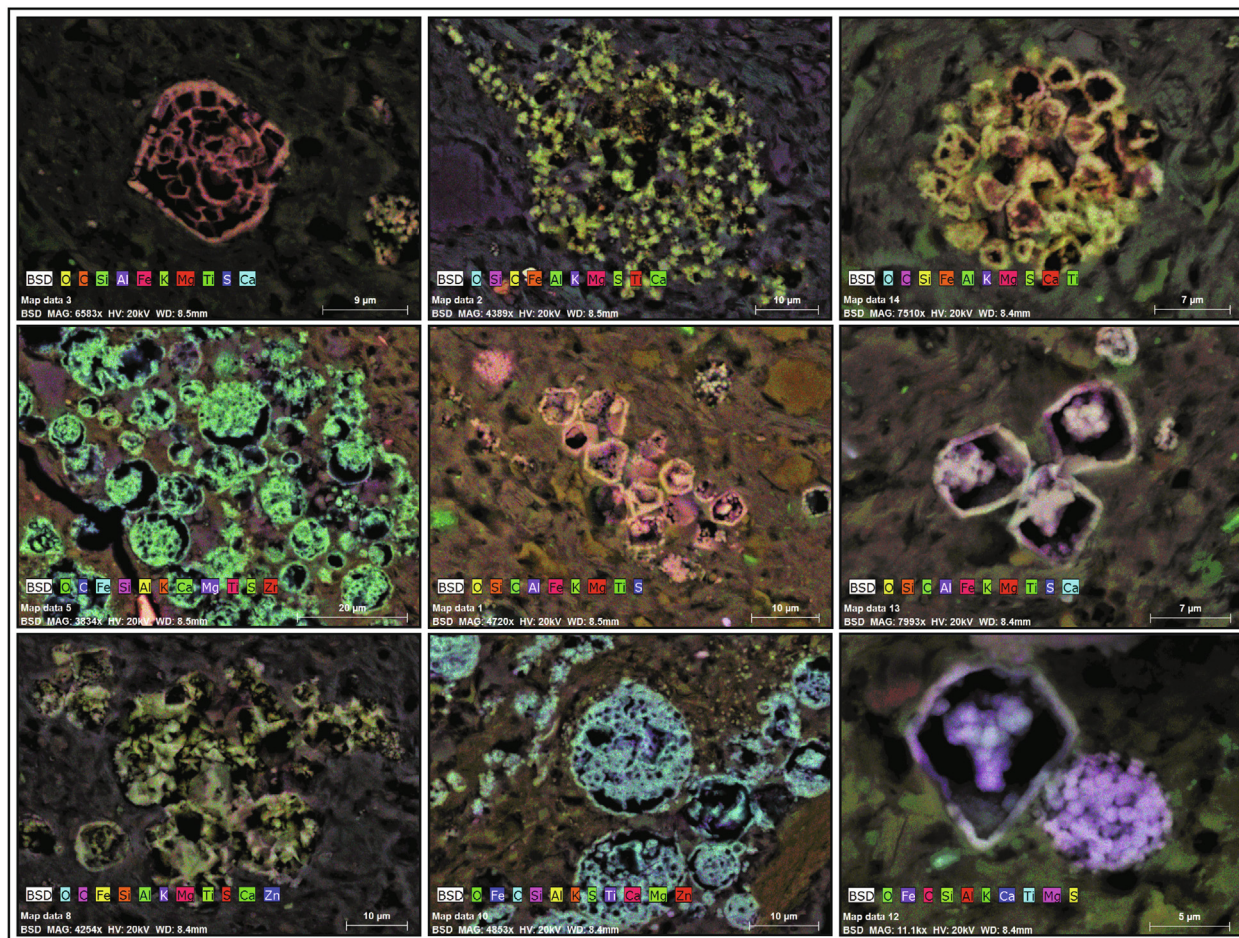


Fig. 10. SEM images of the backscattered-electron signal overlain by false color elemental maps showing pyrite “ghost” crystals altered to iron oxy(hydr)oxide from sample M103-458.3 at 362 m stratigraphic height. (For interpretation of the references to colour in this figure legend, the reader is referred to the web version of this article.)

content and elevated TOC contents and are interpreted to record both a transgressive systems tract and, in some cases, the early regressive systems tract. [Macdonald et al. \(2012\)](#) attributed subsidence to crustal attenuation through the rift-to-drift transition during the early break-up of Rodinia. However, accommodation space need not have been linked to rifting, but rather may have been generated by localized extension followed by thermal subsidence.

## 5.2. Assessment of oxidative weathering effects on bulk-rock iron proxies

A comparative study by [Ahm et al. \(2017\)](#) between fresh drill core and weathered outcrop samples of the Upper Ordovician Vinini Formation in central Nevada, USA provides a template for assessing and predicting weathering trends in iron speciation data. In their study, iron released through pyrite dissolution was predominantly transformed to iron oxy(hydr)oxide, as illustrated by elevated  $Fe_{Oxy}/Fe_{HR}$  ratios and reciprocally reduced  $Fe_{Py}/Fe_{HR}$  ratios in weathered outcrop samples relative to correlative core samples. Although  $Fe_{HR}/Fe_T$  ratios decreased by up

to ~30% for some outcrop samples compared to their stratigraphic equivalents in drill core,  $Fe_T/Al$  ratios were unaffected, indicating the majority of the mobilized  $Fe_{HR}$  pool was transformed to less reactive phases, such as authigenic clay minerals ([Curtis, 1985](#); [Ahm et al., 2017](#)). So, while oxidative weathering can compromise some iron speciation results by lowering  $Fe_{Py}/Fe_{HR}$  values, because pyrite iron is largely transformed to insoluble iron oxy(hydr)oxide and captured locally,  $\delta^{56}Fe$  and  $Fe_T/Al$  proxies preserve their primary composition.

The ubiquitous presence of dissolved pyrite framboid “ghosts” in some samples ([Figs. 10](#) and [S2](#)) indicate that Reefal assemblage samples from section M103 experienced some degree of post-depositional alteration. Although it is difficult to determine when alteration occurred, oxidative weathering following the exhumation of the Wernecke Mountains during the Cordilleran Orogeny may be responsible for the uniformly low  $Fe_{Py}/Fe_{HR}$  values (<0.1) in section M103 from this study ([Figs. 2](#) and [3](#)), as well from many Reefal assemblage sections analyzed by [Sperling et al. \(2013\)](#). Even under non-euxinic conditions, such low  $Fe_{Py}/Fe_{HR}$  values (<0.01) rarely persist over long timescales

in deep water shale depositional environments (Sperling et al., 2015). However, such low pyrite contents may result from low seawater sulfate levels in the late Proterozoic (Kah et al., 2004; Algeo et al., 2015; Fakrae et al., 2019) which would be amplified within a hydrographically restricted basin isolated from the already minimal global marine sulfate reservoir (Berner and Raiswell, 1983; Berner and Raiswell, 1984). Thus, it is difficult to differentiate whether very low  $\text{Fe}_{\text{Py}}/\text{Fe}_{\text{HR}}$  values represent limited sulfide availability, post-depositional oxidative pyrite dissolution, or a combination of the two.

Despite low  $\text{Fe}_{\text{Py}}/\text{Fe}_{\text{HR}}$  from many Reefal assemblage samples across the basin, Sperling et al. (2013) found no petrographic evidence for pyrite dissolution, and sections G0132, G0134, and F845 contain many samples with somewhat elevated  $\text{Fe}_{\text{Py}}/\text{Fe}_{\text{HR}}$ —between 0.2 and 0.8. Analysis of their 231 samples reveal no statistically significant correlation between  $\text{Fe}_{\text{Py}}/\text{Fe}_{\text{HR}}$  and  $\text{Fe}_{\text{HR}}/\text{Fe}_{\text{T}}$  ( $r = 0.15$ ,  $p(\alpha) = 0.025$ ). This confirms that whatever iron was liberated during pyrite dissolution was predominantly transformed to immobile iron oxy(hydr)oxide phases (Fig. 11) in the vicinity of the original pyrite (Fig. S2 and Electronic Annex), similar to observations by Canfield et al. (2008) and Ahm et al. (2017). Furthermore, high  $\text{Fe}_{\text{HR}}/\text{Fe}_{\text{T}}$  values ( $>0.38$ ), which characterize a majority of the samples from

this study, are unlikely to survive if iron was removed via weathering. Considering the low primary pyrite content of most samples, and that dissolved pyrite iron was largely captured locally as iron oxy(hydr)oxides,  $\text{Fe}_{\text{HR}}/\text{Fe}_{\text{T}}$  and  $\text{Fe}_{\text{T}}/\text{Al}$  proxies from the present dataset represent original compositions. In addition, the range in iron isotope values from this study are similar to shale samples of similar age from Svalbard (Kunzmann et al., 2017) and likely do not reflect post-depositional processes. We conclude that while oxidative weathering resulted in pyrite dissolution in some samples from this study, bulk iron proxies (other than  $\text{Fe}_{\text{Py}}/\text{Fe}_{\text{HR}}$ ; i.e.,  $\delta^{56}\text{Fe}$ ,  $\text{Fe}_{\text{HR}}/\text{Fe}_{\text{T}}$ , and  $\text{Fe}_{\text{T}}/\text{Al}$ ) remain robust. The effects of oxidative weathering on RSE proxies are discussed below in Section 5.7.2.

### 5.3. Detrital $\text{Fe}_{\text{T}}/\text{Al}$ baseline

Reefal assemblage shale intervals throughout the basin have consistently low  $\text{Fe}_{\text{T}}/\text{Al}$  ratios ( $\sim 0.2$ ) that exhibit systematic stratigraphic trends that mirror  $\text{Fe}_{\text{HR}}/\text{Fe}_{\text{T}}$  data (Fig. 2; Sperling et al., 2013). The average  $\text{Fe}_{\text{T}}/\text{Al}$  value from section M103 is 0.35 and the average of all sections throughout the basin from Sperling et al. (2013) is 0.37. Both values are low relative to the average upper continental crust ( $\text{Fe}_{\text{T}}/\text{Al}$  of  $\sim 0.48$ ; McLennan, 2001), the composi-

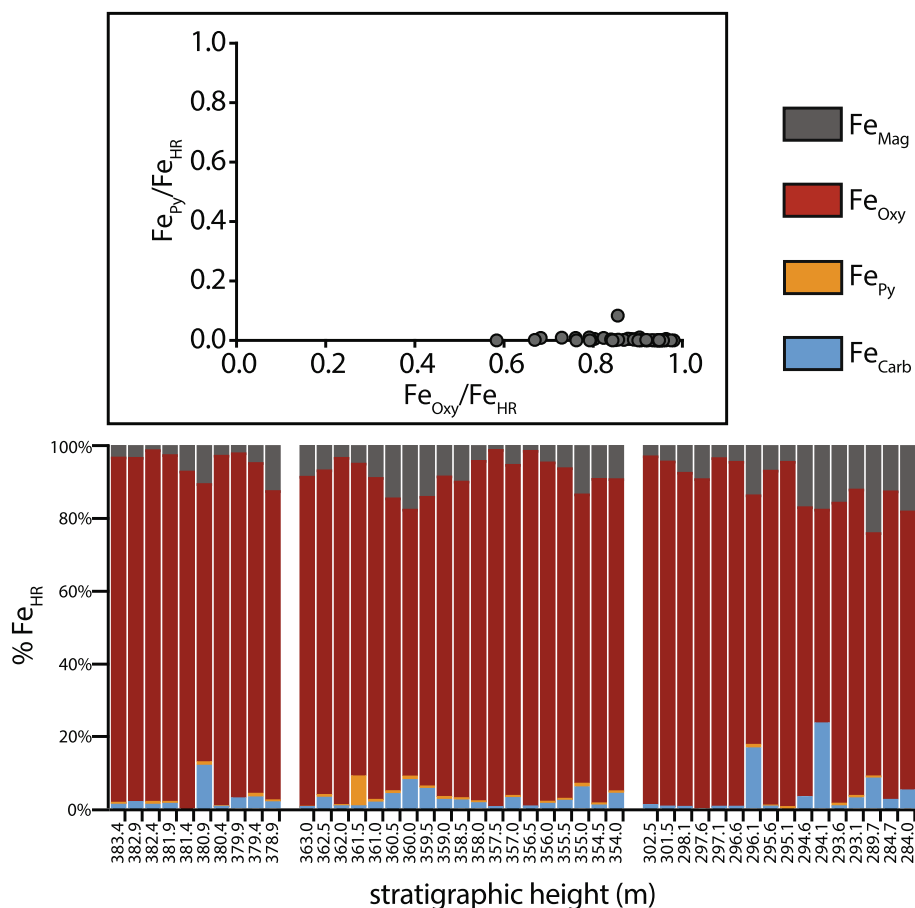


Fig. 11. Cross-plot of  $\text{Fe}_{\text{Oxy}}/\text{Fe}_{\text{HR}}$  versus  $\text{Fe}_{\text{Py}}/\text{Fe}_{\text{HR}}$  (top) and the proportion of  $\text{Fe}_{\text{HR}}$  from  $\text{Fe}_{\text{Carb}}$ ,  $\text{Fe}_{\text{Py}}$ ,  $\text{Fe}_{\text{Oxy}}$  and  $\text{Fe}_{\text{Mag}}$  (bottom). Consistently low  $\text{Fe}_{\text{Py}}/\text{Fe}_{\text{HR}}$  and high  $\text{Fe}_{\text{Oxy}}/\text{Fe}_{\text{HR}}$  values may reflect oxidative weathering of pyrite (Ahm et al., 2017).

tion of which is generally presumed to approximate the average detrital flux to sedimentary basins. It is tempting to ascribe these low  $Fe_T/Al$  values to iron loss via weathering, but any post-depositional, basin-scale alteration is unlikely to remove total iron while retaining high  $Fe_{HR}/Fe_T$ . Furthermore, [Cole et al. \(2017\)](#) reported that the average  $Fe_T/Al$  of partially weathered soil horizons was identical to that of the average upper continental crust. Also,  $Fe_T/Al$  ratios from [Ahm et al. \(2017\)](#) were statistically indistinguishable between weathered and un-weathered samples. In fact, some studies demonstrate iron is enriched within weathering horizons ([Lavergren et al., 2009](#); [Tuttle et al., 2009](#)).

Although  $Fe_T/Al$  values from this study are low compared to the often-cited basin baseline of  $\sim 0.5$ , they are within the compositional range of modern depositional environments. A survey by [Cole et al. \(2017\)](#) found large variability in  $Fe_T/Al$  across active catchments in the USA, and as a result proposed that the  $2\sigma$  confidence interval of  $Fe_T/Al = 0.47 \pm 0.3$  better characterizes the compositional distribution of detrital sedimentary fluxes to sedimentary basins. These data challenge assumptions that detrital  $Fe_T/Al$  compositions are globally homogenous and also highlight the necessity for integrating other proxies for cross-calibration when determining the detrital  $Fe_T/Al$  baseline in an individual basin. Here, we propose a detrital baseline of  $Fe_T/Al \sim 0.3$  for the Reefal assemblage based on integrated relationships with other iron proxy data from this study and [Sperling et al. \(2013\)](#). Namely, samples enriched above this baseline are characterized by  $Fe_{HR}/Fe_T$  values  $> 0.5$ , clearly indicative of authigenic iron enrichment ([Fig. 3](#)). This trend demonstrates that where authigenic iron accumulated, it drove  $Fe_T/Al$  values  $> 0.3$ , suggesting the detrital  $Fe_T/Al$  composition was likely  $\sim 0.3$  or possibly even lower.

It remains unclear why the composition of detrital sedimentary input to certain basins is so low with respect to  $Fe_T/Al$  (e.g., [Sahoo et al., 2012](#)). [Sperling et al. \(2013\)](#) pointed out this phenomenon likely reflects anomalously low detrital iron silicate mineral abundances rather than high aluminum contents. Reducing the total detrital input to the basin would result in reductions in both Fe and Al, so it is more likely low  $Fe_T/Al$  values reflect sediment provenance rather than simply a low detrital flux. Average chemical index of alteration values  $\sim 70$  from the Reefal assemblage imply that these compositions likely do not represent a highly weathered sediment source area. ([Nesbitt and Young, 1982](#); [Sperling et al., 2013](#)). These values also do not reflect dilution by carbonate minerals because low  $Fe_T/Al$  ratios are found in samples with no appreciable carbonate content. Regardless of the exact source of anomalously low sedimentary iron concentrations, deviation from globally averaged values may be more likely in small, restricted basins whose detrital influx is dominantly sourced from a narrow range of lithologies.

We argue that this was likely the case for the Fifteenmile basin, which is consistent with previous interpretations that the Fifteenmile Group was deposited in a series of tectonically active sub basins during localized extension ([Macdonald et al., 2012](#)). It should be noted that no crys-

talline basement is exposed in the surrounding area, nor is there published data from the underlying Wernecke Supergroup that could provide a reference for the source of this anomaly in detrital composition. However, Nd isotope compositions of 17 Reefal assemblage shale samples from [Cox et al. \(2016b\)](#) range from  $\epsilon Nd(t) = -11$  to  $-6$ , with an average  $\epsilon Nd(t) = -8$ . These values are indicative of sediment derived from old, felsic crust, which generally contains low iron concentrations.

#### 5.4. Iron speciation and basin redox

Iron speciation proxies have generally been calibrated from sedimentary environments with detrital  $Fe_T/Al$  baselines that approximate average upper continental crust ([Raiswell and Canfield, 1998](#); [Poulton and Canfield, 2005](#)). Therefore, specific cut-offs may not be suitable for basins with anomalously low  $Fe_T/Al$ . Sediment with low detrital iron concentrations, such as the Reefal assemblage, require a smaller addition of authigenic iron to enrich the highly reactive iron pool relative to total iron. In these cases,  $Fe_{HR}/Fe_T$  values above the 0.38 threshold may not require deposition beneath an anoxic water column. For instance, minor addition of particulate iron oxy(hydr)oxide from reductive dissolution of Fe(II) released from anoxic sediment into an overlying oxic or sub-oxic water column may be able to produce  $Fe_{HR}/Fe_T$  values  $> 0.38$ . Importantly, broad trends in iron speciation from these settings are still dictated by water column redox conditions, so we regard variation in this ratio to reflect changes in depositional redox environment—anoxic waters facilitate greater enrichment of highly reactive iron species relative to oxygenated waters. We therefore implement a more qualitative approach to interpreting iron speciation here.

Although some samples experienced pyrite weathering, the systematic stratigraphic structures displayed in  $Fe_T/Al$ ,  $Fe_{HR}/Fe_T$ , and  $\delta^{56}Fe$  data from this study ([Fig. 2](#)) are unlikely to represent post-depositional Fe mobilization and are therefore interpreted as primary depositional signals. Within samples that retain pyrite and where the crystal habit of framboidal pyrite “ghosts” were preserved (M103-458.3 at 362 m and M103-475.2 at 378.9 m), crystals were variably sized and  $> 5 \mu m$ . Such large, non-uniform pyrite framboids are diagnostic of formation within sediment pore-waters underlying a non-euxinic water column ([Wilkin et al., 1996](#); [Wilkin and Barnes, 1997](#)), so shale samples from this study likely contained relatively low original pyrite content. Similar to [Sperling et al. \(2013\)](#), we interpret samples with high  $Fe_{HR}/Fe_T$  values to have been deposited under an anoxic, primarily ferruginous water column and that  $Fe_{Py}/Fe_{HR}$  ratios were likely  $< 0.8$  before any pyrite dissolution—though brief periods of euxinia cannot be ruled out.

Iron speciation and  $Fe_T/Al$  data through Reefal assemblage transgressive shale intervals are consistent with previous interpretations of the basin redox structure, whereby deep anoxic waters were overlain by oxygenated shallow waters in a redox-stratified water column ([Sperling et al., 2013](#)). Redoxcline transgression during relative sea-level rise manifested as systematic stratigraphic transitions from

low to high  $Fe_{HR}/Fe_T$  and  $Fe_T/Al$  values (i.e., 295–297 m, 355–357 m, 360–362 m and 379–381 m; Fig. 2). Peaks in  $Fe_{HR}/Fe_T$  and  $Fe_T/Al$  ratios at 297, 357, 362 and 381 m are interpreted to represent maximum flooding surfaces. The subsequent steady decline in these proxies reflects shoaling at the start of the regressive systems tract. Based on these proxy trends, two-such redoxcline T-R sequences exist in the second interval between 350–365 m. The first shale interval (280–305 m) does not record redoxcline shoaling following maximum flooding.

Glaucinite is a redox-sensitive mixed-valence iron phyllosilicate that preferentially forms in organic-rich sedimentary environments with low accumulation rates (Cloud et al., 1955). In this study, the high proportion of glaucinite to total illite in samples near the transitions from “oxic” to “anoxic” signatures (i.e., 295, 355, 360 and 379 m; Fig. 2) suggest glaucinite was being formed in the vicinity of the redoxcline (e.g., Tang et al., 2017). Therefore, the redoxcline likely experienced short-term redox fluctuations (O'Brien et al., 1990) superimposed upon sea-level rise during transgressions. Peaks in TOC occur directly below these transitions and then sharply decline, perhaps as a result of increased remineralization triggered by vigorous biogeochemical redox cycling as the redoxcline fluctuated and eventually shoaled during highstand.

### 5.5. Iron isotopes

Experimental and observational studies of iron isotopes in recent decades have elucidated many fractionation pathways and their corresponding fractionation factors. Sedimentary iron isotopes reflect fractionation from redox processes driven both biologically by microbial metabolism (Beard et al., 1999; Beard et al., 2003a; Johnson et al., 2003; Johnson et al., 2004; Matthews et al., 2004; Johnson et al., 2008b) and abiotically (Bullen et al., 2001; Johnson et al., 2002; Beard et al., 2003b; Wiesli et al., 2004; Frierdich et al., 2019). Since there is much overlap in the range of isotope values resulting from each mechanism, discriminating between specific fractionation processes from the sedimentary record poses a significant challenge (Beard and Johnson, 2004). However, the “direction” of fractionation is generally consistent with the “direction” of oxidation state change, regardless of whether the reaction is microbially or abiotically mediated. Heavier isotopes ( $^{56}Fe$  and  $^{57}Fe$ ) are preferentially oxidized while the light isotope ( $^{54}Fe$ ) is preferentially reduced. Although it may not be possible to conclusively differentiate biological versus abiotic fractionation, sedimentary iron isotope signatures offer valuable insight into the modes of redox cycling in depositional environments.

The iron isotope composition of bulk sediment is thought to be controlled by one of two competing mechanisms that fractionate the highly reactive iron pool ( $Fe_{HR}$ ): (1) partial oxidation of aqueous  $Fe(II)$  from the water column or (2) dissimilatory iron reduction (DIR) within the sediment. Because hydrothermal fluids, which have an isotope composition similar to Earth's crust between  $-0.9\%$  and  $+0.1\%$ , likely provided the main source of iron to Proterozoic oceans (Isley, 1995; Bau et al., 1997; Beard

et al., 2003b; Krapez et al., 2003; Severmann et al., 2004; Johnson et al., 2008a; Rouxel et al., 2008; Bennett et al., 2009; Bekker et al., 2010; Klar et al., 2017), deviation from these compositions is generally attributed to one of these two processes.

The first mechanism occurs when anoxic deep waters upwell onto an oxygenated shelf within a redox-stratified ocean or basin, oxidizing some of the aqueous  $Fe(II)$  (e.g., Chever et al., 2015). This process can be either biologically or abiotically mediated. Biological oxidation is associated with a fractionation factor ( $\Delta^{56}Fe_{Fe(II)-Fe(III)}$ ) of ca.  $-1.5\%$  (Croal et al., 2004) and abiotic oxidation an equilibrium fractionation factor of  $-3\%$  (Bullen et al., 2001). Both biological and abiotic fractionation result in an isotopically heavier  $Fe(III)$  product relative to the  $Fe(II)$  reactant through Rayleigh distillation, so the isotope composition of the  $Fe(III)$  product and residual  $Fe(II)$  reservoir are dictated both by the proportion and the initial composition of the  $Fe(II)$  that is oxidized (e.g., Rouxel et al., 2005; Halverson et al., 2011; Planavsky et al., 2012; Chever et al., 2015; Lechte et al., 2019). Therefore, accumulation of iron oxy(hydr)oxide formed by partial oxidation makes sediment isotopically heavier, whereas quantitative oxidation of the aqueous  $Fe(II)$  reservoir imparts no fractionation and the isotope composition of the resulting sediment depends on the initial composition.

The second mechanism relies on DIR, which reductively dissolves isotopically light  $Fe(II)$  from highly reactive iron within anoxic sediment. DIR is associated with a fractionation factor ( $\Delta^{56}Fe_{Fe(II)-Fe(III)}$ ) of  $\sim -3\%$  in both microbially (Beard et al., 1999; Icopini et al., 2004; Crosby et al., 2005; Crosby et al., 2007) and abiotically mediated (Johnson et al., 2002; Welch et al., 2003; Anbar et al., 2005) reactions. The most abundant reactive iron-bearing minerals available for DIR are iron oxy(hydr)oxides. Depending on the proportion of  $Fe(III)$  that is reduced by DIR, the iron isotope composition of the resulting aqueous  $Fe(II)$  is generally between  $1\%$  to  $3\%$  lower than the  $Fe(III)$  substrate (Dauphas et al., 2017), though modelling suggests that when all steps are accounted for (i.e., sorption, etc.) the net isotope fractionation of the  $Fe_{HR}$  pool from diagenetic iron cycling is at most  $\sim 1\%$  (Kunzmann et al., 2017). The  $Fe(II)$  mobilized from DIR can then be shuttled elsewhere in the basin either as aqueous  $Fe(II)$  in a ferruginous water column, pyrite in a euxinic water column or particulate oxy(hydr)oxide in a suboxic water column. In all cases, much of the remobilized iron is transported down-slope or along bathymetric contours and eventually captured within more distal sediment (e.g., Severmann et al., 2006; Severmann et al., 2008; Severmann et al., 2010; Scholz et al., 2014; Scholz et al., 2017).

In order to differentiate which redox-process regulated authigenic iron in a given environment, it is useful to compare the relative iron enrichment or depletion versus iron isotope composition. If partial  $Fe(II)$  oxidation in the water column exerted the dominant control, there should be a positive relationship between  $\delta^{56}Fe$  and  $Fe_T/Al$ , where the slope is dependent on the degree of oxidation of the seawater ferrous iron reservoir. However, analysis of data from

this study reveals a statistically significant negative correlation between  $\delta^{56}\text{Fe}$  and both  $\text{Fe}_T/\text{Al}$  and  $\text{Fe}_{\text{HR}}/\text{Fe}_T$  (Fig. 4). Samples with high  $\text{Fe}_T/\text{Al}$  ( $>0.3$ ) and  $\text{Fe}_{\text{HR}}/\text{Fe}_T$  ( $>0.38$ ) values also have near crustal  $\delta^{56}\text{Fe}$  compositions, and those with low  $\text{Fe}_T/\text{Al}$  ( $<0.3$ ) and  $\text{Fe}_{\text{HR}}/\text{Fe}_T$  ( $<0.38$ ) are  $^{56}\text{Fe}$ -enriched.

Similar trends have been ascribed to particulate shuttling of reactive iron from continental shelves to deeper anoxic basins in the Black Sea (Severmann et al., 2008), open marine environments with low oxygen concentrations (Severmann et al., 2010; Scholz et al., 2014), and in Devonian Appalachian sedimentary basins (Duan et al., 2010; see also Lyons and Severmann, 2006; Lyons et al., 2009). Benthic iron shuttling in the Black Sea produces a negative relationship between  $\delta^{56}\text{Fe}$  and  $\text{Fe}_T/\text{Al}$  because diagenetic reactions such as DIR mobilize isotopically light, highly reactive iron in suboxic shelf sediments, which is subsequently transported to the euxinic basin where it is trapped by syngenetic pyrite and deposited (Wijsman et al., 2001; Andersen and Raiswell, 2004; Lyons and Severmann, 2006; Severmann et al., 2008). In contrast, the  $\delta^{56}\text{Fe}$ - $\text{Fe}_T/\text{Al}$  relationship in the OMZ off the coast of Peru is more complex and the benthic iron shuttle in open marine, non-euxinic settings leads to complex  $\delta^{56}\text{Fe}$ - $\text{Fe}_T/\text{Al}$  relationships. In areas where the OMZ impinges on the seafloor, DIR mobilizes isotopically light iron, which can be transported laterally within the OMZ or downslope and thus removed from the initial depositional site. This leaves sediment depleted in  $\text{Fe}_T/\text{Al}$  and also isotopically heavy (Scholz et al., 2014), much like the trend in data from this study. Although iron mobilized from the OMZ is isotopically light, partial precipitation below the OMZ as iron oxy(hydr)oxide imparts a positive fractionation, and so basinal sediment is characterized by both elevated  $\text{Fe}_T/\text{Al}$  and heavy  $\delta^{56}\text{Fe}$  (Scholz et al., 2014).

The inverse relationships between  $\delta^{56}\text{Fe}$  and both  $\text{Fe}_T/\text{Al}$  and  $\text{Fe}_{\text{HR}}/\text{Fe}_T$  from the Reefal assemblage from this study are consistent with active particulate iron shuttling. However, there are some critical differences compared to previously published data from environments interpreted to experience this phenomenon. Namely, Reefal assemblage samples have lower  $\text{Fe}_T/\text{Al}$  values (as discussed above) and higher  $\delta^{56}\text{Fe}$  values (up to  $\sim 0.8\%$  compared to  $\sim 0.2\%$ ; Severmann et al., 2008 and 2010; Duan et al., 2010; Scholz et al., 2014). Because Reefal assemblage samples with  $\delta^{56}\text{Fe}$  compositions higher than crustal values are also depleted in  $\text{Fe}_T/\text{Al}$  below the detrital baseline, an additional mechanism is necessary to facilitate iron depletion while simultaneously imparting a positive fractionation. Here, we interpret  $\text{Fe}_T/\text{Al}$  depletion below  $\sim 0.3$  coupled with  $\delta^{56}\text{Fe}$  enrichment to represent vigorous dissimilatory iron reduction (DIR), which can lower  $\text{Fe}_T/\text{Al}$  ratios by releasing isotopically light highly reactive Fe(II) (Noffke et al., 2012; Scholz et al., 2014). The low detrital iron content of these shale intervals rendered their bulk iron compositions more sensitive to changes from variation of the  $\text{Fe}_{\text{HR}}$  pool alone. As a result, fractionation from DIR had a greater influence on the bulk  $\delta^{56}\text{Fe}$  compositions of these samples compared to sediment with higher detrital  $\text{Fe}_T/\text{Al}$  (see additional discussion below).

## 5.6. Vigorous dissimilatory iron reduction (DIR) kick-started benthic particulate iron shuttling

Iron-based microbial metabolisms emerged early in Earth's evolutionary history and likely played a significant role in ancient marine iron cycling (Widdel et al., 1993; Konhauser et al., 2002; Kappler et al., 2005; Konhauser et al., 2005; Crowe et al., 2008; Fischer and Knoll, 2009). Dissimilatory iron reduction (DIR) is the only mechanism capable of rendering shale simultaneously depleted in  $\text{Fe}_T/\text{Al}$  relative to the detrital flux and elevated in  $\delta^{56}\text{Fe}$  relative to hydrothermal or crustal values (Fig. 4). At the same time, positive correlation between  $\text{Fe}_T/\text{Al}$  and  $\text{Fe}_{\text{HR}}/\text{Fe}_T$  (Fig. 3) and high  $\text{Fe}_{\text{Oxy}}/\text{Fe}_{\text{HR}}$  values (Fig. 11) requires a flux of highly reactive iron oxy(hydr)oxide through the basin. Highly reactive particulate iron oxy(hydr)oxide can be produced from oxidation of DIR-sourced Fe(II) released from pore-waters where a basin redoxcline impinges the sediment-water interface (van Cappellen et al., 1998; Lyons and Severmann, 2006; Noffke et al., 2012; Scholz et al., 2014). Considering the evidence presented here for relative sea-level change within a redox-stratified basin, we interpret these data to record vigorous benthic particulate iron oxy(hydr)oxide shuttling, stimulated by short-term fluctuations of the basin's redoxcline during high relative sea level.

The high proportion of glauconite to total illite in samples deposited in the vicinity of the redoxcline indicates shorter-term chemical fluctuations during transgression. An oscillating redoxcline, such as from seasonal chemical and density variation, would have promoted a highly variable sedimentary redox environment conducive to dynamic iron cycling. These unique conditions would have generated a positive feedback between active microbial DIR and benthic iron shuttling in the basin. During initial transgression, bio-reactive iron oxy(hydr)oxide particles would have accumulated in recently flooded shelf environments below the shoaling redoxcline. Then, small-scale changes in the depth of the redoxcline would cause the position where the redoxcline impinged the sediment-water interface to sweep back and forth through sediment replete with iron oxy(hydr)oxides and organic matter. In turn, this would generate alternating cycles dominated by DIR and re-accumulation of particulate iron oxy(hydr)oxide.

In the vicinity of the redoxcline, this dynamic redox cycling may have stimulated a thriving microbial community powered by iron-reducing metabolisms and fueled by organic matter accumulation. Vigorous microbial iron reduction near the redoxcline would have rendered the sediment both residually depleted in  $\text{Fe}_T/\text{Al}$  and isotopically heavy (Fig. 4; e.g., Staubwasser et al., 2006; Homoky et al., 2009; Scholz et al., 2014). Thus, peaks in  $\delta^{56}\text{Fe}$  values and minima in  $\text{Fe}_T/\text{Al}$  and  $\text{Fe}_{\text{HR}}/\text{Fe}_T$  (Fig. 2) correspond to maximum removal of isotopically light iron by microbial iron reduction as the redoxcline shoaled during initial transgression. Shuttling and accumulation of isotopically light iron oxy(hydr)oxide below the redoxcline was maximized as the redoxcline continued to shoal, and so  $\delta^{56}\text{Fe}$  minima ( $\sim 0$  to  $+0.1\%$ ) and corresponding peaks in  $\text{Fe}_{\text{HR}}/\text{Fe}_T$ ,  $\text{Fe}_{\text{Oxy}}/\text{Fe}_T$ , and  $\text{Fe}_T/\text{Al}$  mark the maximum flooding sur-

faces of these shale intervals. Thus, maximum flooding surfaces occur at 297 m in the first sampled interval, 357 m and 362 m in the second sampled interval and 381 m in the third sampled interval (Fig. 2). Importantly, while DIR would have needed to reduce a seemingly unreasonable quantity of iron to drive these signals in typical sediment, low detrital iron content in these samples mean that relatively small changes in the isotope composition of their highly reactive iron component is sufficient to affect their bulk  $\delta^{56}\text{Fe}$  composition. Furthermore, iron isotope values from this study are within the upper limits of model predictions for the extent DIR can influence the isotope compositions of highly reactive iron (up to  $\sim 1\%$ ), which require high fluxes of reducible iron (Kunzmann et al., 2017).

### 5.7. Exceptional redox-sensitive element (RSE) enrichments

With the exception of pyrite iron, other iron-based proxies (i.e.,  $\text{Fe}_{\text{HR}}/\text{Fe}_{\text{T}}$  and  $\delta^{56}\text{Fe}$ ) from Reefal assemblage shale samples were largely unaffected by weathering alteration. However, the exceptional RSE enrichments from these samples deserve additional scrutiny. If the unusually high RSE concentrations from this study were to reflect primary depositional signals they would require unprecedented enrichments in Proterozoic sedimentary rocks (up to 5792 ppm Cr, 586 ppm Mn, 726 ppm Mo, and 3509 ppm Ni). Below, we discuss two distinct hypotheses for producing these anomalous enrichments and consider each of their likelihoods for having generated the concentration and distribution of RSEs in Reefal assemblage shale. The first explanation involves RSE adsorption and co-shuttling with Fe-Mn-oxy(hydr)oxide particles, which is a process that has been interpreted to produce extreme Mo and Mn co-enrichments in modern and ancient weakly restricted basins with variable redox conditions. An alternate explanation for the RSE data from the Reefal assemblage is that they were generated by oxidative dissolution, redistribution, and accumulation within the outcrop.

#### 5.7.1. Particulate shuttling and the “Mo pump”?

Dynamic redox cycling due to a fluctuating redoxcline can promote extraordinarily large fluxes of Mo to the sediment through what has been termed the “Mo-pump” by Algeo and Lyons (2006) and Algeo and Tribovillard (2009). Authigenic Mo enrichment in modern sediment exceeding 100 ppm is typically associated with stable euxinic conditions (Scott and Lyons, 2012); however, delivery of Mo to sediment can be enhanced by active iron oxy (hydr)oxide particulate shuttling within weakly restricted basin waters that experience variable redox conditions (Murray, 1975; Magyar et al., 1993; Crusius et al., 1996; Adelson et al., 2001; Dellwig et al., 2010; Scholz et al., 2017). Based on this and previous studies, all of these conditions were met throughout the deposition of Reefal assemblage shale intervals.

This process is thought to involve adsorption of molybdate ( $\text{MoO}_4^{2-}$ ) ions onto Fe-Mn-oxy(hydr)oxide particles under suboxic bottom water conditions and conversion into particle-reactive molybdate ( $\text{MoO}_3$ ), which is then shuttled to the sediment upon sinking (Tribovillard et al., 2012).

Reductive dissolution of these particles during the reappearance of anoxic conditions releases  $\text{MoO}_3$  ions into the sediment where, given sufficient  $\text{H}_2\text{S}$  concentrations, they can be reduced to thiomolybdate ( $\text{MoO}_x\text{S}_{(4-x)}^{2-x}$ ) and be scavenged by organic carbon. Although Mo enrichments require a critical activity of  $\text{H}_2\text{S}$  ( $> \sim 11 \mu\text{M}$ ), peaks in pore-water Mo concentrations often do not correspond to peaks in  $\text{H}_2\text{S}$  (Sundby et al., 2004). Therefore, Mo concentrations do not simply scale with dissolved  $\text{H}_2\text{S}$  concentrations. Rather  $\text{H}_2\text{S}$  may simply function like a “geochemical toggle” whereby a minimum threshold of  $\text{H}_2\text{S}$  concentration is required to produce particle reactive thiomolybdates (Helz et al., 1996), but other mechanisms capable of scavenging these molecules govern the degree to which they are enriched in the sediment.

Comparing relative enrichments between RSEs, TOC and S can shed light on what processes drove chemical fluxes through the basin, and by extension, export to the sediment. For instance, low Mo/TOC, Mo-EF/U-EF, and high TOC/S ratios are indicative of deposition within strongly restricted, euxinic to weakly sulfidic basins due to the “basin reservoir effect” (Algeo and Lyons, 2006), whereby Mo burial outpaces deep water renewal (Berner and Raiswell, 1983; Berner and Raiswell, 1984; Tribovillard et al., 2006; Algeo et al., 2007; Rowe et al., 2008; Algeo and Tribovillard, 2009; Bura-Nakić et al., 2018). Conversely, Mo enrichments due to particulate shuttling can result in distinctively high Mo/TOC (Algeo and Lyons, 2006) and Mo-EF/U-EF ratios (Algeo and Tribovillard, 2009; Tribovillard et al., 2012).

Covariation between Mo-EF and U-EF from Reefal assemblage shale samples display two distinct populations (Fig. 6). Most are not enriched in U with respect to average upper continental crust (U-EF  $\sim 1$ ; McLennan, 2001), but one population ( $n=3$ ) is highly enriched in Mo (Mo-EF  $> 1$ ) and another is relatively depleted (Mo-EF  $< 1$ ). The population enriched in Mo but not enriched in U is characterized by Mo-EF/U-EF ratios up to three times the molar ratio of modern seawater. If primary, such relationships would imply that either late Tonian seawater contained unusually high Mo/U or that Mo was periodically delivered to the sediment with remarkable efficiency. In the latter scenario, extreme co-enrichments of Mo and Mn within high Mo samples (Fig. 7) would suggest that Mn was also involved in the redox cycling and particulate shuttling within basin waters.

If these data reflected a MnO shuttle, this would indicate transport within oxic waters with low  $\text{H}_2\text{S}$  and Fe(II) concentrations (i.e., above the redoxcline; Planavsky et al., 2018). In this case, samples with low Mo/TOC, Mo-EF/U-EF, and high TOC/S ratios from this data set (Figs. 5, 6, 9) result from consistent drawdown of the Mo and S reservoirs due to their efficient removal from the water column following intermittent euxinic conditions that did not persist long enough to produce significant pyrite enrichment in most samples (Berner and Raiswell, 1983; Berner and Raiswell, 1984; Raiswell and Berner, 1985, 1986; Algeo and Tribovillard, 2009; Tribovillard et al., 2012). Then, the extraordinary, but short-lived authigenic Mo enrichments (Mo-EF/U-EF  $> 3 \times$  seawater; Fig. 6)

would represent intermittent episodes of exceptional Mo delivery to the sediment via particulate shuttling from basin waters replete with Mo and S. That these enrichments generally occur at or near the oxic-anoxic transitions, just below the MFS within each flooding interval (i.e., 295, 355, 360, and 379 m stratigraphic heights) and where glauconite to total illite ratios are highest (Fig. 2), might suggest fluctuations in the position of where the redoxcline impinged the sediment water interface may have promoted particulate shuttling. However, the small number of samples with unprecedented RSE concentrations from this dataset suggest that particulate shuttling was unlikely the source of such enrichments.

#### 5.7.2. Redistribution from outcrop weathering?

An alternate and more likely interpretation for the unusually high and somewhat sporadic RSE abundances in select samples from Reefal assemblage shale intervals is that they result from mobilization and redistribution in the outcrop as a result of oxidative weathering. Because pyrite concentrates many RSEs (Huerta-Diaz and Morse, 1992), pyrite dissolution can release high concentrations of RSE into the surrounding rock. Once mobilized via oxidative dissolution or degradation, these elements may be subject to similar chemical reactions as in ancient sedimentary environments. As a result, RSEs released from weathering may accumulate in anoxic regions of weathered outcrops or soil profiles. Furthermore, the strong correlation between Mo and both Cr and Ni in the three highly enriched samples (Fig. 8) could reflect weathering of an ultramafic source. However, low detrital  $Fe_T/Al$  values, highly negative  $\epsilon Nd(t)$  values (Cox et al., 2016b), and the absence of corresponding shifts in Sc/Th ratios do not support provenance from a mafic source (Fig. 2).

Whereas some studies comparing weathered versus unweathered black shale samples show little change in RSE concentrations from oxidative weathering (e.g., Ahm et al., 2017), others demonstrate a wide variety of alteration trends. Elements associated with pyrite or other sulfide minerals are especially prone to mobilization (e.g., Peng et al., 2004; Lavergren et al., 2009; Marynowski et al., 2017). Elements primarily associated with refractory organic matter may be more resistant to weathering (Perkins and Mason, 2015); however, weathering profiles also experience progressive loss of sedimentary organic matter from oxic degradation over longer timescales (Petsch et al. 2000; Wildman et al., 2004), so trace elements associated with sedimentary organic matter are also released into the surrounding rock (e.g., Peng et al., 2004; Tuttle et al., 2009; Marynowski et al., 2017). These investigations reveal non-uniform geochemical behavior in RSEs from shale weathering that is difficult to predict.

Occasionally, RSEs liberated from highly weathered portions of the outcrop concentrate in partially weathered horizons (Tuttle et al., 2009; Marynowski et al., 2017). The simplest explanation for remarkably high Mo, Cr, Ni, and Mn concentrations in Reefal assemblage shale intervals is that these elements accumulated in the outcrop

after being mobilized from pyrite weathering and/or organic matter degradation. In this case, samples with low Mo/TOC and Mo-EF/U-EF but high TOC/S ratios reflect pyrite dissolution and attendant Mo removal rather than a drawdown of Mo and S within the basin reservoir due to hydrographic restriction. As suggested by Marynowski et al. (2017), the preferential dissolution of sulfide minerals during shale weathering may obscure primary RSE signals. Additionally, RSE enrichments in the vicinity of the maximum flooding surfaces (Fig. 2) are likely due to the preferential recapture of these elements within stratigraphic horizons with high TOC values.

Given independent evidence for oxidative pyrite weathering, we accept the most parsimonious hypotheses and interpret the few anomalously high RSE enrichments as products of outcrop weathering rather than cryptic sedimentary processes. However, some combination of the two cannot be entirely ruled out. The strong linear correlation between samples highly enriched in Mo, Ni, Cr, and Mn (Fig. 6) suggests that a common process governed their accumulation after they were mobilized from their original position in the outcrop. Secondary pyrite formation could concentrate some of these elements, but SEM images and iron speciation do not show evidence for any significant pyrite in these samples. There is no clear relationship between the three samples with highest RSE abundance and iron oxy(hydr)oxide nor TOC content, but EDS point analyses from sample M103-475.2, which shows the highest Mo, Ni, Cr, and Mn concentrations, also show Cr, V, Ti, Ni, and Mo peaks within secondary iron oxides after a former pyrite crystal (see Electronic Annex; Figs. S2 and S3). This sample is also the only one from this study with a TOC content > 3% (Fig. 5; Table 1). As a result, a combination of secondary iron oxy(hydr)oxide minerals and organic matter are likely involved in the secondary RSE accumulation in these samples, though additional work is required to fully understand the mechanisms involved. Importantly, RSE data from this study likely does not reflect primary, depositional redox conditions.

## 6. CONCLUSIONS

In this study, we integrate a high-resolution, multi-proxy geochemical dataset from Reefal assemblage shale intervals with a sequence stratigraphic model to elucidate dynamics of basin's redox structure, as well as iron cycling just prior to major perturbations in global carbon cycling (e.g., Halverson et al., 2005; Halverson et al., 2007; Swanson-Hysell et al., 2015), eukaryotic diversification (Cohen and Macdonald, 2015) and the emergence of animals (Berney and Pawlowski, 2006; Erwin et al., 2011; Parfrey et al., 2011; Dohrmann and Worheide, 2017). Iron isotope and iron speciation data across each shale interval display distinct stratigraphic trends interpreted to reflect redoxcline fluctuations within a redox-stratified basin during relative sea-level change. These coherent, systematic trends and their similarity to iron speciation data from throughout the basin from Sperling et al. (2013) support

a model in which the surface layer in the Fifteenmile basin was oxic while deep waters were anoxic and predominantly ferruginous.

The unusually low  $\text{Fe}_T/\text{Al}$  composition ( $\sim 0.3$ ) of the detrital flux to the Fifteenmile basin and other recent studies of modern and ancient sediment geochemistry challenge the common assumption that detrital  $\text{Fe}_T/\text{Al}$  compositions are homogenous globally. This finding highlights the need to establish detrital  $\text{Fe}_T/\text{Al}$  baselines on a case-by-case basis rather than assuming a composition based on upper continental crust or various shale composition averages. Furthermore, iron speciation proxies have largely been calibrated in settings with initial  $\text{Fe}_T/\text{Al}$  values  $\sim 0.5$  and the traditional threshold of  $\text{Fe}_{\text{HR}}/\text{Fe}_T > 0.38$  as an indicator of anoxic deposition may not be suitable for samples from environments with unusually low detrital  $\text{Fe}_T/\text{Al}$  baselines.

Isotope modeling of the iron cycle by Kunzmann et al. (2017) suggested that water column processes, i.e., the delivery of iron oxy(hydr)oxide particles, controls the  $\delta^{56}\text{Fe}$  composition of the highly reactive pool, and therefore bulk shale. However, Kunzmann et al. (2017) found an overall weak negative relationship in their Neoproterozoic sample set between  $\delta^{56}\text{Fe}$  and  $\text{Fe}_T/\text{Al}$ , as well as between  $\delta^{56}\text{Fe}$  and both  $\text{Fe}_{\text{HR}}/\text{Fe}_T$  and  $\text{Fe}_{\text{Oxy}}/\text{Fe}_T$ . This relationship was most strongly developed in samples from the Reefal assemblage—and further bolstered by new data reported herein. We interpret these negative relationships and the stratigraphic patterns from the Reefal assemblage to record enhanced redox cycling from vigorous DIR-driven benthic iron shuttling stimulated by short-term fluctuations in the redoxcline during relative sea level highs. Thus, although water column iron cycling may control the bulk iron isotope composition of shale from many environments, low  $\text{Fe}/\text{Al}$  values amplified the influence of diagenetic redox cycling on the bulk iron isotope compositions of Reefal assemblage shale intervals.

Finally, anomalously high concentrations of certain RSEs from a few samples from this study are hard to explain by depositional or early diagenetic processes alone, despite the fact that they mimic certain geochemical relationships indicative of the basin-reservoir effect or co-shuttling of reactive trace metals. Rather, we attribute unusually high RSE values to enrichment within the outcrop following mobilization by oxidative weathering. This process generated enrichments that could be misinterpreted as an expansion of marine RSE inventories due to global oxygenation. Considering the widespread implementation of RSE compilations for studies interested in tracking the secular redox evolution of Earth's surface, this study serves as a cautionary tale highlighting the detrimental effects of weathering alteration on redox-sensitive geochemical proxies.

### Declaration of Competing Interest

The authors declare that they have no known competing financial interests or personal relationships that could have appeared to influence the work reported in this paper.

### ACKNOWLEDGEMENTS

The Yukon Geological Survey, Natural Sciences and Engineering Research Council of Canada, Polar Continental Shelf Program, and the Yukon Foundation provided logistical and financial support for this research. We acknowledge the Tr'ondëk Hwech'in First Nation for permitting us to conduct fieldwork on their traditional lands. TMG also acknowledges support from the Eric Mountjoy Legacy Scholarship and the Agouron Geobiology Fellowship. MK acknowledges support through various scholarships awarded by the Department of Earth and Planetary Sciences at McGill University and Geotop. We thank Eric Bellefroid for help in the field and also Geoff Gilleaudeau, Bjorn Sundby, Noah Planavsky, Erik Sperling, Austin Miller, Max Lechte, Malcolm Hodgskiss, Peter Crockford and Boswell Wing for discussions about this dataset. Constructive and thorough reviews from Thomas Algeo, Andrey Bekker, and an anonymous reviewer improved this manuscript greatly. We also thank associate editor Silke Severmann and executive editor Jeffrey Catalano for additional helpful comments and editorial handling.

### APPENDIX A. SUPPLEMENTARY MATERIAL

Supplementary data to this article can be found online at <https://doi.org/10.1016/j.gca.2020.04.013>.

### REFERENCES

- Adelson J. M., Helz G. R. and Miller C. V. (2001) Reconstructing the rise of recent coastal anoxia; molybdenum in Chesapeake Bay sediments. *Geochim. Cosmochim. Acta* **65**(2), 237–252.
- Ader M., Sansjofre P., Halverson G. P., Busigny V., Trindade R. I. F., Kunzmann M. and Nogueira A. C. R. (2014) Ocean redox structure across the Late Neoproterozoic Oxygenation Event: a nitrogen isotope perspective. *Earth and Planet. Sci. Lett.* **396**(C), 1–13.
- Ahm A. S. C., Bjerrum C. J. and Hammarlund E. U. (2017) Disentangling the record of diagenesis, local redox conditions, and global seawater chemistry during the latest Ordovician glaciation. *Earth and Planet. Sci. Lett.* **459**, 145–156.
- Algeo T. J. (2004) Can marine anoxic events draw down the trace element inventory of seawater? *Geology* **32**(12), 1057–1054.
- Algeo T. J. and Lyons T. W. (2006) Mo–total organic carbon covariation in modern anoxic marine environments: implications for analysis of paleoredox and paleohydrographic conditions. *Paleoceanography* **21**, PA1016.
- Algeo T. J., Lyons T. W., Blakey R. C. and Over D. J. (2007) Hydrographic conditions of the Devonian–Carboniferous North American Seaway inferred from sedimentary Mo–TOC relationships. *Palaeogeogr. Palaeoclimatol. Palaeoecol.* **256**(3–4), 204–230.
- Algeo T. J. and Tribouillard N. (2009) Environmental analysis of paleoceanographic systems based on molybdenum–uranium covariation. *Chem. Geol.* **268**(3–4), 211–225.
- Algeo T. J., Luo G. M., Song H. Y., Lyons T. W. and Canfield D. E. (2015) Reconstruction of secular variation in seawater sulfate concentrations. *Biogeosci. Discuss.* **12**(7), 2131–2151.
- Anbar A. D., Jarzecki A. A. and Spiro T. G. (2005) Theoretical investigation of iron isotope fractionation between  $\text{Fe}(\text{H}_2\text{O})_6^{3+}$  and  $\text{Fe}(\text{H}_2\text{O})_6^{2+}$ : implications for iron stable isotope geochemistry. *Geochim. Cosmochim. Acta* **69**(4), 825–837.
- Anbar A. D. and Rouxel O. (2007) Metal stable isotopes in paleoceanography. *Annu. Rev. Earth Planet. Sci.* **35**(1), 717–746.

- Andersen T. and Raiswell R. (2004) Sources and mechanisms for the enrichment of highly reactive iron in euxinic Black Sea sediments. *Am. J. Sci.* **304**(3), 203–231.
- Bau M., Hohndorf A., Dulski P. and Beukes N. J. (1997) Sources of rare-earth elements and iron in paleoproterozoic iron-formations from the Transvaal Supergroup, South Africa: evidence from neodymium isotopes. *J. Geol.* **105**(1), 121–129.
- Beard B. L. and Johnson C. M. (2004) Fe isotope variations in the modern and ancient earth and other planetary bodies. *Rev. Mineral. Geochem.* **55**, 319–357.
- Beard B. L., Johnson C. M., Cox L., Sun H., Neelson K. H. and Aguilar C. (1999) Iron isotope biosignatures. *Science* **285**(5435), 1889–1892.
- Beard B. L., Johnson C. M., Skulan J. L., Neelson K. H., Cox L. and Sun H. (2003a) Application of Fe isotopes to tracing the geochemical and biological cycling of Fe. *Chem. Geol.* **195**(1–4), 87–117.
- Beard B. L., Johnson C. M., Von Damm K. L. and Poulson R. L. (2003b) Iron isotope constraints on Fe cycling and mass balance in oxygenated Earth oceans. *Geology* **31**(7), 629–632.
- Bekker A., Holland H. D., Wang P. L., Rumble D., Stein H. J., Hannah J. L., Coetzee L. L. and Beukes N. J. (2004) Dating the rise of atmospheric oxygen. *Nature* **427**(6970), 117–120.
- Bekker A., Slack J. F., Planavsky N., Krapez B., Hofmann A., Konhauser K. O. and Rouxel O. J. (2010) Iron formation: the sedimentary product of a complex interplay among mantle, tectonic, oceanic, and biospheric processes. *Econ. Geol.* **105**(3), 467–508.
- Bennett S. A., Rouxel O., Schmidt K., Garbe-Schonberg D., Statham P. J. and German C. R. (2009) Iron isotope fractionation in a buoyant hydrothermal plume, 5 degrees S Mid-Atlantic Ridge. *Geochim. Cosmochim. Acta* **73**(19), 5619–5634.
- Berner R. A. and Raiswell R. (1983) Burial of Organic-Carbon and Pyrite Sulfur in Sediments over Phanerozoic Time – a New Theory. *Geochim. Cosmochim. Acta* **47**(5), 855–862.
- Berner R. A. and Raiswell R. (1984) C/S method for distinguishing freshwater from marine sedimentary rocks. *Geology* **12**(6), 365–368.
- Berney C. and Pawlowski J. (2006) A molecular time-scale for eukaryote evolution recalibrated with the continuous microfossil record. *Proc. Biol. Sci.* **273**(1596), 1867–1872.
- Blamey N. J. F., Brand U., Parnell J., Spear N., Lecuyer C., Benison K., Meng F. W. and Ni P. (2016) Paradigm shift in determining Neoproterozoic atmospheric oxygen. *Geology* **44**(8), 651–654.
- Brumsack H. J. (2006) The trace metal content of recent organic carbon-rich sediments: implications for Cretaceous black shale formation. *Palaeogeogr. Palaeoclimatol. Palaeoecol.* **232**(2–4), 344–361.
- Bullen T. D., White A. F., Childs C. W., Vivit D. V. and Schulz M. S. (2001) Demonstration of significant abiotic iron isotope fractionation in nature. *Geology* **29**(8), 699–702.
- Bura-Nakić E., Andersen M. B., Archer C., Souza G. F. d., Margus M. and Vance D. (2018) Coupled Mo-U abundances and isotopes in a small marine euxinic basin: constraints on processes in euxinic basins. *Geochim. Cosmochim. Acta* **222**, 212–229.
- Canfield D. E., Raiswell R., Westrich J. T., Reaves C. M. and Berner R. A. (1986) The use of chromium reduction in the analysis of reduced inorganic sulfur in sediments and shales. *Chem. Geol.* **54**(1–2), 149–155.
- Canfield D. E., Poulton S. W., Knoll A. H., Narbonne G. M., Ross G., Goldberg T. and Strauss H. (2008) Ferruginous conditions dominated later neoproterozoic deep-water chemistry. *Science* **321**(5891), 949–952.
- Canfield D. E., Poulton S. W. and Narbonne G. M. (2007) Late-Neoproterozoic deep-ocean oxygenation and the rise of animal life. *Science* **315**(5808), 92–95.
- Canfield D. E., Zhang S., Frank A. B., Wang X., Wang H., Su J., Ye Y. and Frei R. (2018) Highly fractionated chromium isotopes in Mesoproterozoic-aged shales and atmospheric oxygen. *Nat. Commun.* **9**(1), 2871.
- Chever F., Rouxel O. J., Croot P. L., Ponzevera E., Wuttig K. and Auro M. (2015) Total dissolvable and dissolved iron isotopes in the water column of the Peru upwelling regime. *Geochim. Cosmochim. Acta* **162**, 66–82.
- Cloud, Jr., P. E. (1955) Physical limits on the glauconite formation. *Am. Assoc. Pet. Geol. Bull.* **39**(4), 484–492.
- Cohen P. A. and Macdonald F. A. (2015) The Proterozoic Record of Eukaryotes. *Paleobiology* **41**(4), 610–632.
- Cole D. B., Reinhard C. T., Wang X. L., Gueguen B., Halverson G. P., Gibson T., Hodgskiss M. S. W., McKenzie N. R., Lyons T. W. and Planavsky N. J. (2016) A shale-hosted Cr isotope record of low atmospheric oxygen during the Proterozoic. *Geology* **44**(7), 555–558.
- Cole D. B., Zhang S. and Planavsky N. J. (2017) A new estimate of detrital redox-sensitive metal concentrations and variability in fluxes to marine sediments. *Geochim. Cosmochim. Acta* **215**, 337–353.
- Cox G. M., Jarrett A., Edwards D., Crockford P. W., Halverson G. P., Collins A. S., Poirier A. and Li Z. X. (2016a) Basin redox and primary productivity within the Mesoproterozoic Roper Seaway. *Chem. Geol.* **440**, 101–114.
- Cox G. M., Halverson G. P., Stevenson R. K., Vokaty M., Poirier A., Kunzmann M., Li Z. X., Denyszyn S. W., Strauss J. V. and Macdonald F. A. (2016b) Continental flood basalt weathering as a trigger for Neoproterozoic Snowball Earth. *Earth Planet. Sci. Lett.* **446**, 89–99.
- Craig H. (1957) Isotopic standards for carbon and oxygen and correction factors for mass-spectrometric analysis of carbon dioxide. *Geochim. Cosmochim. Acta* **12**(1–2), 133–149.
- Croal L. R., Johnson C. M., Beard B. L. and Newman D. K. (2004) Iron isotope fractionation by Fe(II)-oxidizing photoautotrophic bacteria. *Geochim. Cosmochim. Acta* **68**(6), 1227–1242.
- Crosby H. A., Johnson C. M., Roden E. E. and Beard B. L. (2005) Coupled Fe(II)-Fe(III) electron and atom exchange as a mechanism for Fe isotope fractionation during dissimilatory iron oxide reduction. *Environ. Sci. Technol.* **39**(17), 6698–6704.
- Crosby H. A., Roden E. E., Johnson C. M. and Beard B. L. (2007) The mechanisms of iron isotope fractionation produced during dissimilatory Fe(III) reduction by *Shewanella putrefaciens* and *Geobacter sulfurreducens*. *Geobiology* **5**(2), 169–189.
- Crowe S. A., Jones C., Katsev S., Magen C., O'Neill A. H., Sturm A., Canfield D. E., Haffner G. D., Mucci A., Sundby B. and Fowle D. A. (2008) Photoferrotrophs thrive in an Archean Ocean analogue. *PNAS* **105**(41), 15938–15943.
- Crusius J., Calvert S., Pedersen T. and Sage D. (1996) Rhenium and molybdenum enrichments in sediments as indicators of oxic, suboxic and sulfidic conditions of deposition. *Earth Planet. Sci. Lett.* **145**(1–4), 65–78.
- Curtis C. D. (1985) Clay mineral precipitation and transformation during burial diagenesis. *Philos. Trans. A Math. Phys. Eng. Sci.* **315**(1531), 91–105.
- Dahl T. W., Hammarlund E. U., Anbar A. D., Bond D. P., Gill B. C., Gordon G. W., Knoll A. H., Nielsen A. T., Schovsbo N. H.

- and Canfield D. E. (2010) Devonian rise in atmospheric oxygen correlated to the radiations of terrestrial plants and large predatory fish. *PNAS* **107**(42), 17911–17915.
- Dauphas N., John S. G. and Rouxel O. (2017) Iron Isotope Systematics. *Rev. Mineral. Geochem.* **82**(1), 415–510.
- Dauphas N. and Rouxel O. (2006) Mass spectrometry and natural variations of iron isotopes. *Mass Spectrom. Rev.* **25**(4), 515–550.
- Dellwig O., Leipe T., Marz C., Glockzin M., Pollehne F., Schnetger B., Yakushev E. V., Bottcher M. E. and Brumsack H. J. (2010) A new particulate Mn-Fe-P-shuttle at the redox-cline of anoxic basins. *Geochim. Cosmochim. Acta* **74**(24), 7100–7115.
- Diamond C., Planavsky N., Wang C. and Lyons T. (2018) What the ~1.4 Ga Xiamaling Formation can and cannot tell us about the mid-Proterozoic ocean. *Geobiology* **16**(3), 219–236.
- Dohrmann M. and Worheide G. (2017) Dating early animal evolution using phylogenomic data. *Sci. Rep.* **7**(1), 3599.
- Duan Y., Severmann S., Anbar A. D., Lyons T. W., Gordon G. W. and Sageman B. B. (2010) Isotopic evidence for Fe cycling and repartitioning in ancient oxygen-deficient settings: examples from black shales of the mid-to-late Devonian Appalachian basin. *Earth Planet. Sci. Lett.* **290**(3–4), 244–253.
- Emerson S. R. and Huested S. S. (1991) Ocean Anoxia and the Concentrations of Molybdenum and Vanadium in Seawater. *Mar. Chem.* **34**(3–4), 177–196.
- Erwin D. H., Laflamme M., Tweedt S. M., Sperling E. A., Pisani D. and Peterson K. J. (2011) The Cambrian conundrum: early divergence and later ecological success in the early history of animals. *Science* **334**(6059), 1091–1097.
- Fakraee M., Hancisse O., Canfield D. E., Crowe S. A. and Katsev S. (2019) Proterozoic seawater sulfate scarcity and the evolution of ocean–atmosphere chemistry. *Nat. Geosci.* **12**(5), 375–380.
- Fan H. F., Zhu X. K., Wen H. J., Yan B., Li J. and Feng L. J. (2014) Oxygenation of Ediacaran Ocean recorded by iron isotopes. *Geochim. Cosmochim. Acta* **140**, 80–94.
- Fischer W. W. and Knoll A. H. (2009) An iron shuttle for deep water silica in Late Archean and early Paleoproterozoic iron formation. *Geol. Soc. Am. Bull.* **121**(1–2), 222–235.
- Friedrich A. J., Nebel O., Beard B. L. and Johnson C. M. (2019) Iron isotope exchange and fractionation between hematite ( $\alpha$ -Fe<sub>2</sub>O<sub>3</sub>) and aqueous Fe(II): a combined three-isotope and reversal-approach to equilibrium study. *Geochim. Cosmochim. Acta* **245**, 207–221.
- Gilleaudeau G. J., Frei R., Kaufman A. J., Kah L. C., Azmy K., Bartley J. K., Chernyavskiy P. and Knoll A. H. (2016) Oxygenation of the mid-Proterozoic atmosphere: clues from chromium isotopes in carbonates. *Geochem. Perspect. Lett.* **2**(2), 178–186.
- Gilleaudeau G. J. and Kah L. C. (2015) Heterogeneous redox conditions and a shallow chemocline in the Mesoproterozoic ocean: evidence from carbon-sulfur-iron relationships. *Precamb. Res.* **257**, 94–108.
- Guilbaud R., Poulton S. and Butterfield N., et al. (2015) A global transition to ferruginous conditions in the early Neoproterozoic oceans. *Nature Geoscience* **8**, 466–470.
- Halverson G. P., Hoffman P. F., Schrag D. P., Maloof A. C. and Rice A. H. N. (2005) Toward a Neoproterozoic composite carbon-isotope record. *Geol. Soc. Am. Bull.* **117**(9–10), 1181–1207.
- Halverson G. P., Macdonald F. A., Strauss J. V., Smith E. F., Cox G. M. and Hubert-Théou L. (2012) Updated definition and correlation of the lower Fifteenmile Group in the central and eastern Ogilvie Mountains. In *Yukon Exploration and Geology* (eds. K. E. MacFarlane and P. J. Sack). Geological Survey, Yukon, pp. 75–90.
- Halverson G. P., Maloof A. C., Schrag D. P., Dudas F. O. and Hurtgen M. (2007) Stratigraphy and geochemistry of a ca 800 Ma negative carbon isotope interval in northeastern Svalbard. *Chem. Geol.* **237**(1–2), 5–27.
- Halverson G. P., Poitrasson F., Hoffman P. F., Nédélec A., Montel J. M. and Kirby J. (2011) Fe isotope and trace element geochemistry of the Neoproterozoic syn-glacial Rapitan iron formation. *Earth Planet. Sci. Lett.* **309**(1–2), 100–112.
- Hardisty D. S., Lu Z. L., Planavsky N. J., Bekker A., Philippot P., Zhou X. L. and Lyons T. W. (2014) An iodine record of Paleoproterozoic surface ocean oxygenation. *Geology* **42**(7), 619–622.
- Helz G. R., Miller C. V., Charnock J. M., Mosselmans J. F. W., Patrick R. A. D., Garner C. D. and Vaughan D. J. (1996) Mechanism of molybdenum removal from the sea and its concentration in black shales: EXAFS evidence. *Geochim. Cosmochim. Acta* **60**(19), 3631–3642.
- Homoky W. B., Severmann S., Mills R. A., Statham P. J. and Fones G. R. (2009) Pore-fluid Fe isotopes reflect the extent of benthic Fe redox recycling: evidence from continental shelf and deep-sea sediments. *Geology* **37**(8), 751–754.
- Huerta-Diaz M. A. and Morse J. W. (1992) Pyritization of trace metals in anoxic marine sediments. *Geochim. Cosmochim. Acta* **56**(7), 2681–2702.
- Icopini G. A., Anbar A. D., Ruebush S. S., Tien M. and Brantley S. L. (2004) Iron isotope fractionation during microbial reduction of iron: the importance of adsorption. *Geology* **32**(3), 205–208.
- Isley A. E. (1995) Hydrothermal Plumes and the Delivery of Iron to Banded Iron-Formation. *J. Geol.* **103**(2), 169–185.
- Jochum K. P., Nohl U., Herwig K., Lammel E., Stoll B. and Hofmann A. W. (2005) GeoReM: a new geochemical database for reference materials and isotopic standards. *Geostand. Geoanal. Res.* **29**(3), 333–338.
- Johnson C. M. and Beard B. L. (2005) Biogeochemical cycling of iron isotopes. *Science* **309**(5737), 1025–1027.
- Johnson C. M., Beard B. L., Beukes N. J., Klein C. and O’Leary J. M. (2003) Ancient geochemical cycling in the Earth as inferred from Fe isotope studies of banded iron formations from the Transvaal Craton. *Contrib. Miner. Petrol.* **144**(5), 523–547.
- Johnson C. M., Beard B. L., Klein C., Beukes N. J. and Roden E. E. (2008a) Iron isotopes constrain biologic and abiologic processes in banded iron formation genesis. *Geochim. Cosmochim. Acta* **72**(1), 151–169.
- Johnson C. M., Beard B. L. and Roden E. E. (2008b) The iron isotope fingerprints of redox and biogeochemical cycling in the modern and ancient Earth. *Annu. Rev. Earth Planet. Sci.* **36**(1), 457–493.
- Johnson C. M., Beard B. L., Roden E. E., Newman D. K. and Neelson K. H. (2004) Isotopic constraints on biogeochemical cycling of Fe. *Rev. Mineral. Geochem.* **55**, 359–408.
- Johnson C. M., Skulan J. L., Beard B. L., Sun H., Neelson K. H. and Braterman P. S. (2002) Isotopic fractionation between Fe (III) and Fe(II) in aqueous solutions. *Earth and Planet. Sci. Lett.* **195**(1–2), 141–153.
- Johnston D. T., Poulton S. W., Dehler C., Porter S., Husson J., Canfield D. E. and Knoll A. H. (2010) An emerging picture of Neoproterozoic ocean chemistry: insights from the Chuar Group, Grand Canyon, USA. *Earth and Planet. Sci. Lett.* **290**(1–2), 64–73.
- Kah L. C., Lyons T. W. and Frank T. D. (2004) Low marine sulphate and protracted oxygenation of the Proterozoic biosphere. *Nature* **431**(7010), 834–838.
- Kappler A., Pasquero C., Konhauser K. O. and Newman D. K. (2005) Deposition of banded iron formations by anoxygenic

- phototrophic Fe(II)-oxidizing bacteria. *Geology* **33**(11), 865–868.
- Klar J. K., James R. H., Gibbs D., Lough A., Parkinson I., Milton J. A., Hawkes J. A. and Connelly D. P. (2017) Isotopic signature of dissolved iron delivered to the Southern Ocean from hydrothermal vents in the East Scotia Sea. *Geology* **45**(4), 351–354.
- Knoll A. H. (2014) Paleobiological perspectives on early eukaryotic evolution. *Cold Spring Harb. Perspect. Biol.* **6**(1), a016121.
- Konhauser K. O., Hamade T., Raiswell R., Morris R. C., Grant Ferris F., Southam G. and Canfield D. E. (2002) Could bacteria have formed the Precambrian banded iron formations? *Geology* **30**(12), 1079–1082.
- Konhauser K. O., Newman D. K. and Kappler A. (2005) The potential significance of microbial Fe(III) reduction during deposition of Precambrian banded iron formations. *Geobiology* **3**(3), 167–177.
- Krapez B., Barley M. E. and Pickard A. L. (2003) Hydrothermal and resedimented origins of the precursor sediments to banded iron formation: sedimentological evidence from the Early Palaeoproterozoic Brockman Supersequence of Western Australia. *Sedimentology* **50**(5), 979–1011.
- Kunzmann M., Gibson T. M., Halverson G. P., Hodgskiss M. S. W., Bui T. H., Carozza D. A., Sperling E. A., Poirier A., Cox G. M. and Wing B. A. (2017) Iron isotope biogeochemistry of Neoproterozoic marine shales. *Geochim. Cosmochim. Acta* **209**, 85–105.
- Kunzmann M., Halverson G.P., Macdonald F.A., Hodgskiss M., Sansjofre P.D., Schumann, D. and Rainbird R.H. (2014) The early Neoproterozoic Chandindu Formation of the Fifteenmile Group in the Ogilvie Mountains. In *Yukon Exploration and Geology 2013* (eds. K.E. MacFarlane, M.G. Nordling, and P.J. Sack) Yukon Geological Survey, pp. 93–107.
- Kunzmann M., Halverson G. P., Scott C., Minarik W. G. and Wing B. A. (2015) Geochemistry of Neoproterozoic black shales from Svalbard: implications for oceanic redox conditions spanning Cryogenian glaciations. *Chem. Geol.* **417**, 383–393.
- Lavergren U., Åström M. E., Bergbäck B. and Holmström H. (2009) Mobility of trace elements in black shale assessed by leaching tests and sequential chemical extraction. *Geochem. Explor. Env. Anal.* **9**(1), 71–79.
- Lechte M. A., Wallace M. W., van Smeerdijk Hood A., Li W., Jiang G., Halverson G. P., Asael D., McColl S. L. and Planavsky N. J. (2019) Subglacial meltwater supported aerobic marine habitats during Snowball Earth. *PNAS* **116**(51), 35478–25483.
- Liu X. M., Kah L. C., Knoll A. H., Cui H., Kaufman A. J., Shahar A. and Hazen R. M. (2016) Tracing Earth's O<sub>2</sub> evolution using Zn/Fe ratios in marine carbonates. *Geochem. Perspect. Lett.* **2** (1), 24–34.
- Lu W., Ridgwell A., Thomas E., Hardisty D. S., Luo G., Algeo T. J., Saltzman M. R., Gill B. C., Shen Y., Ling H. F. and Edwards C. T. (2018) Late inception of a resiliently oxygenated upper ocean. *Science* **361**(6398), 174–177.
- Lyons T. W., Anbar A. D., Severmann S., Scott C. and Gill B. C. (2009) Tracking euxinia in the ancient ocean: a multiproxy perspective and proterozoic case study. *Annu. Rev. Earth and Planet. Sci.* **37**(1), 507–534.
- Lyons T. W. and Severmann S. (2006) A critical look at iron paleoredox proxies: new insights from modern euxinic marine basins. *Geochim. Cosmochim. Acta* **70**(23), 5698–5722.
- Macdonald F. A., Halverson G. P., Strauss J. V., Smith E. F., Cox G., Sperling E. A. and Roots C. F. (2012) Early Neoproterozoic Basin Formation in Yukon, Canada: implications for the make-up and break-up of Rodinia. *Geosci. Can.* **39**, 77–99.
- Macdonald F. A. and Roots C. F. (2010) Upper Fifteenmile Group in the Ogilvie Mountains and correlations of early Neoproterozoic strata in the northern Cordillera. In *Yukon Exploration and Geology 2009* (eds. K. E. MacFarlane, L. H. Weston and L. R. Blackburn). Yukon Geological Survey, Whitehorse, YT, pp. 237–252.
- Macdonald F. A., Schmitz M. D., Crowley J. L., Roots C. F., Jones D. S., Maloof A. C., Strauss J. V., Cohen P. A., Johnston D. T. and Schrag D. P. (2010) Calibrating the Cryogenian. *Science* **327**(5970), 1241–1243.
- Macdonald F. A., Schmitz M. D., Strauss J. V., Halverson G. P., Gibson T. M., Eyster A., Cox G., Mamrol P. and Crowley J. L. (2018) Cryogenian of Yukon. *Precamb. Res.* **319**, 114–143.
- Macdonald F. A., Smith E. F., Strauss J. V., Cox G. M., Halverson G. P. and Roots C. F. (2011) Neoproterozoic and early Paleozoic correlations in the western Ogilvie Mountains, Yukon. In *Yukon Exploration and Geology 2010* (eds. K. E. MacFarlane, L. H. Weston and C. Relf). Whitehorse, Yukon Geological Survey, pp. 161–182.
- Magyar B., Moor H. C. and Sigg L. (1993) Vertical-Distribution and Transport of Molybdenum in a Lake with a Seasonally Anoxic Hypolimnion. *Limnol. and Oceanogr.* **38**(3), 521–531.
- Marynowski L., Pisarzowska A., Derkowski A., Rakociński M., Szaniawski R., Śródoń J. and Cohen A. S. (2017) Influence of palaeoweathering on trace metal concentrations and environmental proxies in black shales. *Palaeogeogr. Palaeoclimatol. Palaeoecol.* **472**, 177–191.
- Matthews A., Morgans-Bell H. S., Emmanuel S., Jenkyns H. C., Erel Y. and Halicz L. (2004) Controls on iron-isotope fractionation in organic-rich sediments (Kimmeridge Clay, Upper Jurassic, southern England). *Geochim. Cosmochim. Acta* **68**(14), 3107–3123.
- McLennan S. M. (2001) Relationships between the trace element composition of sedimentary rocks and upper continental crust. *Geochem. Geophys. Geosyst.* **2**, 1–24.
- Medig K. P. R., Thorkelson D. J., Davis W. J., Gibson H. D., Rainbird R. H. and Marshall D. D. (2012) The Proterozoic Pinguicula Group, Wernecke Mountains, Yukon: a siliciclastic and carbonate slope to basin succession with local and exotic sediment provenance. In *Yukon Exploration and Geology* (eds. MacFarlane, K. E., Weston, L. H., and Relf, C.) Yukon Geological Survey, p. 1–22.
- Murray J. W. (1975) The interaction of metal ions at the manganese dioxide-solution interface. *Geochim. Cosmochim. Acta* **39**(4), 505–519.
- Nesbitt H. W. and Young G. M. (1982) Early Proterozoic climates and plate motions inferred from major element chemistry of lutites. *Nature* **299**(5885), 715–717.
- Noffke A., Hensen C., Sommer S., Scholz F., Bohlen L., Mosch T., Graco M. and Wallmann K. (2012) Benthic iron and phosphorus fluxes across the Peruvian oxygen minimum zone. *Limnol. Oceanogr.* **57**(3), 851–867.
- Odin G. S., Velde B. and Bonhomme M. (1977) Radiogenic argon in glauconites as a function of mineral recrystallization. *Earth Planet. Sci. Lett.* **37**, 154–158.
- O'Brien G. W., Milnes A. R., Veeh H. H., Heggie D. T., Riggs S. R., Cullen D. J., Marshall J. F. and Cook P. J. (1990) Sedimentation Dynamics and Redox Iron-Cycling—Controlling Factors for the Apatite-Glauconite Association on the East Australian Continental-Margin. *Geol. Soc. Spec. Pub.* **52**(1), 61–86.
- Parfrey L. W., Lahr D. J., Knoll A. H. and Katz L. A. (2011) Estimating the timing of early eukaryotic diversification with multigene molecular clocks. *PNAS* **108**(33), 13624–13629.
- Partin C. A., Lalonde S. V., Planavsky N. J., Bekker A., Rouxel O. J., Lyons T. W. and Konhauser K. O. (2013) Uranium in iron

- formations and the rise of atmospheric oxygen. *Chem. Geol.* **362**, 82–90.
- Peng B., Song Z., Tu X., Xiao M., Wu F. and Lv H. (2004) Release of heavy metals during weathering of the Lower Cambrian black shales in western Hunan. *China. Environ. Geol.* **45**(8), 1137–1147.
- Perkins R. B. and Mason C. E. (2015) The relative mobility of trace elements from short-term weathering of a black shale. *Appl. Geochem.* **56**, 67–79.
- Petsch S. T., Berner R. A. and Eglinton T. I. (2000) A field study of the chemical weathering of ancient sedimentary organic matter. *Org. Geochem.* **31**(5), 475–487.
- Planavsky N. J., Cole D. B., Reinhard C. T., Diamond C., Love G. D., Luo G., Zhang S., Konhauser K. O. and Lyons T. W. (2016) No evidence for high atmospheric oxygen levels 1,400 million years ago. *PNAS* **113**(19), E2550–E2551.
- Planavsky N. J., McGoldrick P., Scott C. T., Li C., Reinhard C. T., Kelly A. E., Chu X., Bekker A., Love G. D. and Lyons T. W. (2011) Widespread iron-rich conditions in the mid-Proterozoic ocean. *Nature* **477**(7365), 448–451.
- Planavsky N. J., Reinhard C. T., Wang X., Thomson D., McGoldrick P., Rainbird R. H., Johnson T., Fischer W. W. and Lyons T. W. (2014) Low mid-Proterozoic atmospheric oxygen levels and the delayed rise of animals. *Science* **346**(6209), 635–638.
- Planavsky N. J., Slack J. F., Cannon W. F., O’Connell B., Isson T. T., Asael D., Jackson J. C., Hardisty D. S., Lyons T. W. and Bekker A. (2018) Evidence for episodic oxygenation in a weakly redox-buffered deep mid-Proterozoic ocean. *Chem. Geol.* **483**, 581–594.
- Planavsky N., Rouxel O. J., Bekker A., Hofmann A., Little C. T. S. and Lyons T. W. (2012) Iron isotope composition of some Archean and Proterozoic iron formations. *Geochim. Cosmochim. Acta* **80**(C), 158–169.
- Poulton S. W. and Canfield D. E. (2005) Development of a sequential extraction procedure for iron: implications for iron partitioning in continentally derived particulates. *Chem. Geol.* **214**(3–4), 209–221.
- Poulton S. W. and Canfield D. E. (2011) Ferruginous conditions: a dominant feature of the ocean through earth’s history. *Elements* **7**(2), 107–112.
- Poulton S. W., Fralick P. W. and Canfield D. E. (2010) Spatial variability in oceanic redox structure 1.8 billion years ago. *Nat. Geosci.* **3**(7), 486–490.
- Poulton S. W. and Raiswell R. (2002) The low-temperature geochemical cycle of iron: from continental fluxes to marine sediment deposition. *Am. J. Sci.* **302**(9), 774–805.
- Rainbird R. H., McNicoll V. J., Thériault R. J., Heaman L. M., Abbott J. G., Long D. G. F. and Thorkelson D. J. (1997) Pancontinental River System Draining Grenville Orogen Recorded by U-Pb and Sm-Nd Geochronology of Neoproterozoic Quartzarenites and Mudrocks, Northwestern Canada. *J. Geol.* **105**, 1–17.
- Raiswell R. and Berner R. A. (1985) Pyrite Formation in Euxinic and Semi-Euxinic Sediments. *Am. J. Sci.* **285**(8), 710–724.
- Raiswell R. and Berner R. A. (1986) Pyrite and Organic-Matter in Phanerozoic Normal Marine Shales. *Geochim. Cosmochim. Acta* **50**(9), 1967–1976.
- Raiswell R. and Berner R. A. (1987) Organic carbon losses during burial and thermal maturation of normal marine shales. *Geology* **15**, 853–856.
- Raiswell R. and Canfield D. E. (1998) Sources of iron for pyrite formation in marine sediments. *Am. J. Sci.* **298**(3), 219–245.
- Reinhard C. T., Planavsky N. J., Robbins L. J., Partin C. A., Gill B. C., Lalonde S. V., Bekker A., Konhauser K. O. and Lyons T. W. ( ) Proterozoic ocean redox and biogeochemical stasis. *PNAS* **110**(14), 5357–5362.
- Rooney A. D., Strauss J. V., Brandon A. D. and Macdonald F. A. (2015) A Cryogenian chronology: two long-lasting synchronous Neoproterozoic glaciations. *Geology* **43**(5), 459–462.
- Rouxel O., Shanks W. C., Bach W. and Edwards K. J. (2008) Integrated Fe- and S-isotope study of seafloor hydrothermal vents at East Pacific rise 9–10 degrees N. *Chem. Geol.* **252**(3–4), 214–227.
- Rouxel O. J. and Auro M. (2010) Iron Isotope Variations in Coastal Seawater Determined by Multicollector ICP-MS. *Geostan. Geoanal. Res.* **34**(2), 135–144.
- Rouxel O. J., Bekker A. and Edwards K. J. (2005) Iron isotope constraints on the Archean and Paleoproterozoic ocean redox state. *Science* **307**(5712), 1088–1091.
- Rowe H. D., Loucks R. G., Ruppel S. C. and Rimmer S. M. (2008) Mississippian Barnett Formation, Fort Worth Basin, Texas: bulk geochemical inferences and Mo-TOC constraints on the severity of hydrographic restriction. *Chem. Geol.* **257**(1–2), 16–25.
- Sahoo S. K., Planavsky N. J., Kendall B., Wang X., Shi X., Scott C., Anbar A. D., Lyons T. W. and Jiang G. (2012) Ocean oxygenation in the wake of the Marinoan glaciation. *Nature* **489**(7417), 546–549.
- Scholz F., Severmann S., McManus J. and Hensen C. (2014) Beyond the Black Sea paradigm: the sedimentary fingerprint of an open-marine iron shuttle. *Geochim. Cosmochim. Acta* **127**, 368–380.
- Scholz F., Siebert C., Dale A. W. and Frank M. (2017) Intense molybdenum accumulation in sediments underneath a nitrogenous water column and implications for the reconstruction of paleo-redox conditions based on molybdenum isotopes. *Geochim. Cosmochim. Acta* **213**, 400–417.
- Scott C. and Lyons T. W. (2012) Contrasting molybdenum cycling and isotopic properties in euxinic versus non-euxinic sediments and sedimentary rocks: refining the paleoproxies. *Chem. Geol.* **324**(C), 19–27.
- Scott C., Lyons T. W., Bekker A., Shen Y., Poulton S. W., Chu X. and Anbar A. D. (2008) Tracing the stepwise oxygenation of the Proterozoic ocean. *Nature* **452**(7186), 456–459.
- Severmann S., Johnson C. M., Beard B. L., German C. R., Edmonds H. N., Chiba H. and Green D. R. H. (2004) The effect of plume processes on the Fe isotope composition of hydrothermally derived Fe in the deep ocean as inferred from the Rainbow vent site, Mid-Atlantic Ridge, 36 degrees 14’ N. *Earth Plan. Sci. Lett.* **225**(1–2), 63–76.
- Severmann S., Johnson C. M., Beard B. L. and McManus J. (2006) The effect of early diagenesis on the Fe isotope compositions of porewaters and authigenic minerals in continental margin sediments. *Geochim. Cosmochim. Acta* **70**(8), 2006–2022.
- Severmann S., Lyons T. W., Anbar A., McManus J. and Gordon G. (2008) Modern iron isotope perspective on the benthic iron shuttle and the redox evolution of ancient oceans. *Geology* **36**(6), 487–490.
- Severmann S., McManus J., Berelson W. M. and Hammond D. E. (2010) The continental shelf benthic iron flux and its isotope composition. *Geochim. Cosmochim. Acta* **74**(14), 3984–4004.
- Snyder R. and Bish D. L. (1989) Quantitative analysis. *Rev. Mineral. Geochem.* **20**(1), 101–144.
- Sossi P. A., Halverson G. P., Nebel O. and Eggins S. M. (2015) Combined separation of Cu, Fe and Zn from rock matrices and improved analytical protocols for stable isotope determination. *Geostand. Geoanal. Res.* **39**(2), 129–149.
- Sperling E. A. and Stockey R. G. (2018) The temporal and environmental context of early animal evolution: considering all

- the ingredients of an “Explosion”. *Integr. Comp. Biol.* **58**(4), 605–622.
- Sperling E. A., Halverson G. P., Knoll A. H., Macdonald F. A. and Johnston D. T. (2013) A basin redox transect at the dawn of animal life. *Earth Plan. Sci. Lett.* **371**(C), 143–155.
- Sperling E. A., Rooney A. D., Hays L., Sergeev V. N., Vorob'eva N. G., Sergeeva N. D., Selby D., Johnston D. T. and Knoll A. H. (2014) Redox heterogeneity of subsurface waters in the Mesoproterozoic ocean. *Geobiology* **12**(5), 373–386.
- Sperling E. A., Wolock C. J., Morgan A. S., Gill B. C., Kunzmann M., Halverson G. P., Macdonald F. A., Knoll A. H. and Johnston D. T. (2015) Statistical analysis of iron geochemical data suggests limited late Proterozoic oxygenation. *Nature* **523** (7561), 451–454.
- Srodon J., Drits V. A., McCarty D. K., Hsieh J. C. and Eberl D. D. (2001) Quantitative X-ray diffraction analysis of clay-bearing rocks from random preparations. *Clays Clay Miner.* **49**(6), 514–528.
- Staubwasser M., von Blanckenburg F. and Schoenberg R. (2006) Iron isotopes in the early marine diagenetic iron cycle. *Geology* **34**(8), 629–632.
- Strauss J. V., Macdonald F. A., Halverson G. P., Tosca N. J., Schrag D. P. and Knoll A. H. (2015) Stratigraphic evolution of the neoproterozoic callison lake formation: linking the break-up of rodnia to the islay carbon isotope excursion. *Am. J. Sci.* **315**(10), 881–944.
- Strauss J. V., Roots C. F., Macdonald F. A., Halverson G. P., Eyster A. and Colpron M. (2014) Geological map of the Coal Creek inlier, Ogilvie Mountains (NTS 116B/10-15 and 116C/9,16): 1:100,000 scale.
- Sundby B., Martinez P. and Gobeil C. (2004) Comparative geochemistry of cadmium, rhenium, uranium, and molybdenum in continental margin sediments. *Geochim. Cosmochim. Acta* **68**(11), 2485–2493.
- Swanson-Hysell N. L., Maloof A. C., Condon D. J., Jenkin G. R. T., Alene M., Tremblay M. M., Tesema T., Rooney A. D. and Haileab B. (2015) Stratigraphy and geochronology of the Tambien Group, Ethiopia: evidence for globally synchronous carbon isotope change in the Neoproterozoic. *Geology* **43**(4), 323–326.
- Tang D., Xiaoying S., Ma J., Jiang G., Zhou X. and Shi Q. (2017) Formation of shallow-water glaucony in weakly oxygenated Precambrian ocean: an example from the Mesoproterozoic Tieling Formation in North China. *Precamb. Res.* **294**, 214–229.
- Tribouillard N., Algeo T. J., Baudin F. and Riboulleau A. (2012) Analysis of marine environmental conditions based on molybdenum–uranium covariation—Applications to Mesozoic paleoceanography. *Chem. Geol.* **324**, 46–58.
- Tribouillard N., Algeo T. J., Lyons T. and Riboulleau A. (2006) Trace metals as paleoredox and paleoproductivity proxies: an update. *Chem. Geol.* **232**(1–2), 12–32.
- Tuttle M. L. W., Breit G. N. and Goldhaber M. B. (2009) Weathering of the New Albany Shale, Kentucky: II. Redistribution of minor and trace elements. *Appl. Geochem.* **24**(8), 1565–1578.
- van Cappellen P., Viollier E., Roychoudhury A., Clark L., Ingall E., Lowe K. and Dichristina T. (1998) Biogeochemical cycles of manganese and iron at the oxic-anoxic transition of a stratified marine basin (Orca Basin, Gulf of Mexico). *Environ. Sci. Technol.* **32**(19), 2931–2939.
- Velde B. and Odin G. S. (1975) Further information related to the origin of glauconite. *Clays Clay Mineral.* **23**, 376–381.
- Wallace M. W., Hood A. V. S., Shuster A., Greig A., Planavsky N. J. and Reed C. P. (2017) Oxygenation history of the Neoproterozoic to early Phanerozoic and the rise of land plants. *Earth Planet. Sci. Lett.* **466**, 12–19.
- Welch S. A., Beard B. L., Johnson C. M. and Braterman P. S. (2003) Kinetic and equilibrium Fe isotope fractionation between aqueous Fe(II) and Fe(III). *Geochim. Cosmochim. Acta* **67**(22), 4231–4250.
- Widdel F., Schnell S., Heising S., Ehrenreich A., Assmus B. and Schink B. (1993) Ferrous Iron Oxidation by Anoxygenic Phototrophic Bacteria. *Nature* **362**(6423), 834–836.
- Wiesli R., Beard B. and Johnson C. (2004) Experimental determination of Fe isotope fractionation between aqueous Fe (II), siderite and “green rust” in abiotic systems. *Chem. Geol.* **211**(3–4), 343–362.
- Wijsman J. W. M., Middelburg J. J. and Heip C. H. R. (2001) Reactive iron in Black Sea Sediments: implications for iron cycling. *Mar. Geol.* **172**(3–4), 167–180.
- Wildman R. A., Berner R. A., Petsch S. T., Bolton E. W., Eckert J. O., Mok U. and Evans J. B. (2004) The weathering of sedimentary organic matter as a control on atmospheric O<sub>2</sub>: I. Analysis of a black shale. *Am. J. Sci.* **304**(3), 234–249.
- Wilkin R. T. and Barnes H. L. (1997) Formation processes of framboidal pyrite. *Geochim. Cosmochim. Acta* **61**(2), 323–339.
- Wilkin R. T., Barnes H. L. and Brantley S. L. (1996) The size distribution of framboidal pyrite in modern sediments. An indicator of redox conditions. *Geochim. Cosmochim. Acta* **60** (20), 3897–3912.
- Yueng L. Y. (2017) Low oxygen and argon in the Neoproterozoic atmosphere at 815 Ma. *Earth Planet. Sci. Lett.* **480**, 66–74.
- Zhang F. F., Zhu X. K., Yan B., Kendall B., Peng X., Li J., Algeo T. J. and Romaniello S. (2015) Oxygenation of a Cryogenian ocean (Nanhua Basin, South China) revealed by pyrite Fe isotope compositions. *Earth Planet. Sci. Lett.* **429**(C), 11–19.
- Zhang S., Wang X., Wang H., Bjerrum C. J., Hammarlund E. U., Haxen E. R., Wen H., Ye Y. and Canfield D. E. (2019) Paleoenvironmental proxies and what the Xiamaling Formation tells us about the mid-Proterozoic ocean. *Geobiology* **17**(3), 225–246.
- Zhang S., Wang X., Wang H., Bjerrum C. J., Hammarlund E. U., Costa M. M., Connelly J. N., Zhang B., Su J. and Canfield D. E. (2016a) Sufficient oxygen for animal respiration 1,400 million years ago. *PNAS* **113**(7), 1731–1736.
- Zhang S., Wang X., Wang H., Bjerrum C. J., Hammarlund E. U., Dahl T. W. and Canfield D. E. (2016b) Reply to Planavsky et al.: strong evidence for high atmospheric oxygen levels 1,400 million years ago. *PNAS* **113**(19), E2552–E2553.